

Zero-Power PEMS System with Full-Bridge PWM Inverter: from Mechanism to Algorithm

Zeyi ZHANG (✉ zhangzy@jxust.edu.cn)

Jiangxi University of Science and Technology

Research Article

Keywords: permanent-electro magnetic suspension (PEMS), attractive magnetic force, Full-Bridge PWM Inverter, pulse-width-modulation (PWM)

Posted Date: May 27th, 2021

DOI: <https://doi.org/10.21203/rs.3.rs-558587/v1>

License:   This work is licensed under a Creative Commons Attribution 4.0 International License.

[Read Full License](#)

Version of Record: A version of this preprint was published at IEEE Access on April 6th, 2022. See the published version at <https://doi.org/10.1109/ACCESS.2022.3165307>.

Zero-Power PEMS System with Full-Bridge PWM Inverter: from Mechanism to Algorithm

Zeyi Zhang^{1,*}

¹ School of Electrical Engineering and Automation, Jiangxi University of Science and Technology, Ganzhou, China

* email: zhangzy@jxust.edu.cn

ABSTRACT

The permanent-electro magnetic suspension (PEMS) technology takes advantage of the attractive magnetic force between the magnet and the iron core and reduces the power consumption eventually to zero. However, the current of the zero-power PEMS system fluctuates around zero due to disturbances and suffers from the electronic nonlinearity. This work presents that the 2 μ s turn-off delay (*one electronic defect*) of the integrated circuit (IC) L298N (*one commercial full-bridge pulse-width-modulation (PWM) inverter produced by STMicroelectronics*) leads to the nonlinear current-duty cycle characteristic, which undermines the control stability and limits the PWM frequency of the zero-power PEMS system. Moreover, the nonlinear mechanism is experimentally and theoretically analyzed for the critical PWM frequency and the sensitivity transition. Furthermore, this work proposes the compensation algorithm to overcome the electronic nonlinearity. It is demonstrated that the three-piece linearization approach stabilizes the PEMS system with only a few milliamperere current and outperforms the two-piece counterpart with stronger robustness and smoother dynamics under the current-step-change test, especially for the PWM frequency higher than the critical value. Besides, the breakthrough of the critical PWM frequency by the compensation algorithm is of great significance for the dynamic performance of the high-speed PEMS transportation system.

Introduction

The electromagnetic suspension (EMS) technology has played an essential role in the maglev transportation industry in Germany, Japan, and China since 1960s¹. Besides, the active magnetic bearing² is another successful application of the EMS technology and is widely found in flywheel systems, high-speed

drives, and turbomolecular pumps. However, the EMS technology consumes considerable large power to generate sufficient attractive force ³ and requires high-performance electronics, such as the isolated gate bipolar transistor (IGBT) ⁴ and the LLC resonant converter ⁵.

In 1980s, the Nd-Fe-B permanent magnet was invented as a special functional material with the largest magnetic energy accumulation. Since then, the permanent-electro magnetic suspension (PEMS) technology ³ is economically effective by using the Nd-Fe-B permanent magnet to produce the attractive force and reduce the power consumption eventually to zero ⁶, whereas the electromagnet only plays a dynamic regulatory role ⁴. Mizuno and *et al.* ⁷ developed an active vibration isolation system with an infinite stiffness against disturbances based on the zero-power PEMS technology. Zhang and *et al.* ⁸ numerically optimized the geometry for the zero-power PEMS system as undergraduate project kits in terms of the zero-power force and the controller-gain requirement.

Due to its outstanding energy-saving and robust features, the zero-power PEMS technology also attracted great attention from the maglev transportation industry. Tzeng and Wang ⁹ presented a rigorous dynamic analysis for the high-speed maglev transportation system with the robust zero-power PEMS strategy. Zhang and *et al.* ⁴ focused on the optimal structural design of the PEMS magnet and proposed optimized parameters with better carrying capability and lower suspension power loss. Cho and *et al.* ¹⁰ reported a successful quadruple PEMS system with the improved zero-power control algorithm.

Importantly, unlike the non-zero-mean current (I) in the EMS technology ^{11,12}, the current for the zero-power PEMS technology fluctuates about zero due to external disturbances ^{10,13}. Though the full-bridge pulse-width-modulation (PWM) inverter ² (also known as the power converter ¹⁴ or the chopper ³) can drive the zero-mean current in the electromagnet according to the PWM duty cycle (D), there are few works analyzing its electronic nonlinearity that could be one of the most critical factors for the zero-power PEMS technology.

Moreover, the sampling rate (f_{sample}) and the PWM frequency (f_{PWM}) are two crucial parameters for the dynamic performance of the high-speed PEMS transportation system, e.g., the disturbance rejection and the gap tracking ¹⁵. In the literature, f_{sample} is usually set from 75 Hz to 2 kHz ^{12,16-18} for the digital controller, whereas f_{PWM} is usually set from 10 kHz to 20 kHz ^{3,11-13}. Generally, f_{sample} is at least 5-time smaller than f_{PWM} . Hence, in order to enhance the dynamic performance of the high-speed PEMS transportation system, higher f_{PWM} is under huge demand but may amplify the electronic nonlinearity of the full-bridge PWM inverter.

This work aims to analyze the electronic nonlinearity of the full-bridge PWM inverter for the zero-power PEMS system. The paper starts with the preliminaries of the single-axis PEMS system. Then, the nonlinear mechanism of the $I - D$ characteristic is analyzed. Moreover, two piecewise linearization approaches are

compared under the current-step-change test for two f_{PWM} with respect to (w.r.t.) the critical PWM frequency (f_{cr}). Nevertheless, discussion is addressed.

Results

Preliminaries

This subsection addresses the preliminaries of the single-axis PEMS system. Firstly, the experimental setup is detailed with the hardware and the three nonlinear relationships. Secondly, the current in the electromagnet is theoretically modelled. Thirdly, the nonlinear $I - D$ characteristic of the full-bridge PWM inverter with the electromagnet is briefly presented and to be further analyzed and compensated in the present work.

Experimental setup

Figure 1 visualizes the close-loop architecture of the single-axis PEMS system, Figure 2 visualizes the associated hardware, and Table 1 lists out physical properties. The six elements are:

- 1) Floater includes the payload and the Nd-Fe-B permanent magnet with the grade of N35. The magnet holder keeps the minimum gap between the magnet and the iron core to protect the ITR8307 sensor, while the three vertical rods and the soft connection maintains the upwards orientation of the magnet regardless of the gravity center of the payload;
- 2) ITR8307 distance sensor converts the floating height (h) between the floater and the electromagnet into the height signal (U_h) by the reflection intensity of the infra light. Besides, a light-proof housing is installed to entirely cover the single-axis PEMS system;
- 3) Analog signal processor converts U_h into the proportional and differential signals (U_p and U_d);
- 4) Digital STM32 controller outputs the PWM signal with f_{PWM} and D (based on U_p , U_d and the double-loop control algorithm). Besides, the real-time data are upload to the computer by the serial port;
- 5) L298N full-bridge PWM inverter converts the PWM signal into I through the electromagnet. I is measured by the ammeter, while the voltage across the electromagnet is measured by the oscilloscope; and
- 6) Electromagnet generates the attractive magnetic force (F) on the magnet to balance the gravity (G) of the floater.

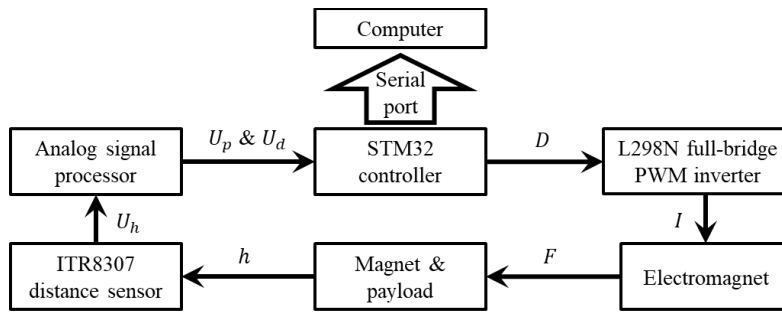


Figure 1. Close-loop architecture of the single-axis PEMS system.

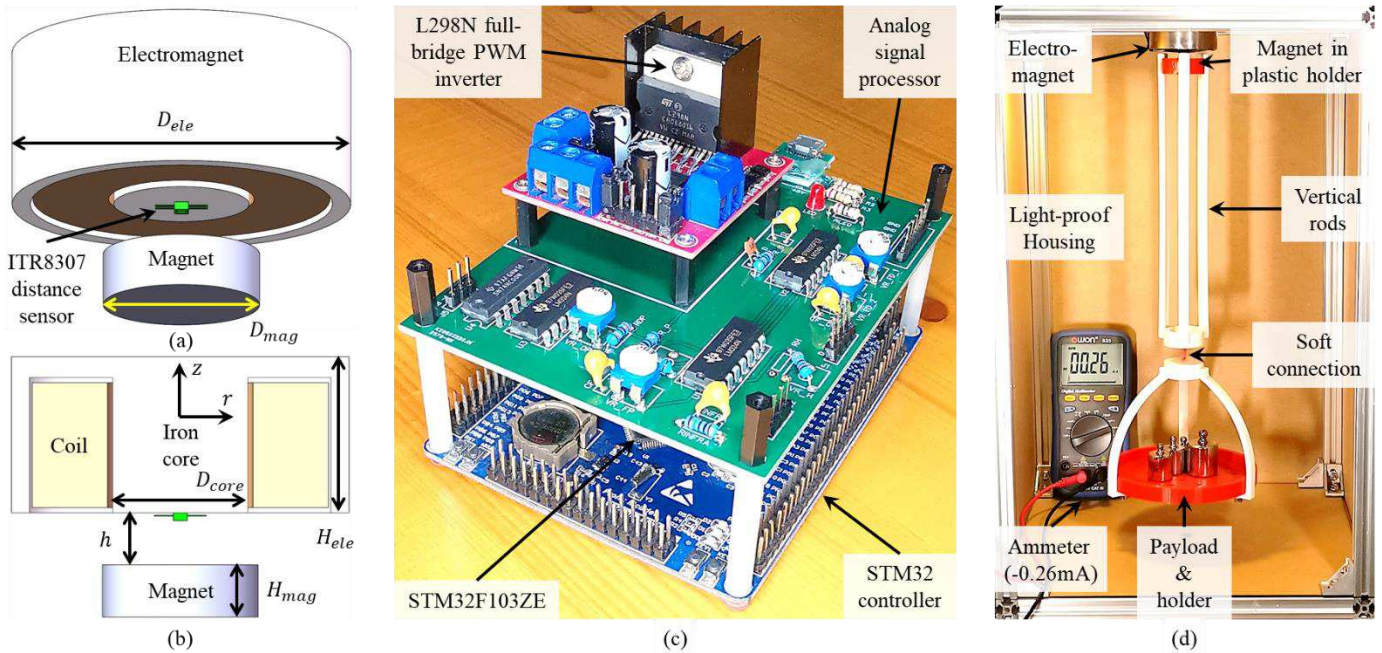


Figure 2. Hardware of the single-axis PEMS system, (a) stereoscopic view and (b) cross-sectional view for the electromagnet and the permanent magnet, (c) electronic devices, and (d) experiment rig.

Symbols	Quantity	Value	Unit
m	Floater mass	0.76	kg
M	Electromagnet mass	0.59	kg
R	Electromagnet resistor	14.5	Ω
U	Power supply voltage	12	V
f_{PWM}	PWM frequency	0.1~100	kHz
f_{cr}	Critical PWM frequency	15.28	kHz
T	PWM period	0.01~10	ms
f_{sample}	Controller sampling rate	200	Hz
D_{mag}	Magnet diameter	30	mm
H_{mag}	Magnet thickness	10	mm
D_{ele}	Electromagnet outer diameter	65	mm
D_{core}	Electromagnet iron-core diameter	26	mm
H_{ele}	Electromagnet thickness	30	mm
h	Floating height	9.5~10.9	mm

Table 1. Physical properties of the single-axis PEMS system.

Moreover, there are three nonlinear relationships for the single-axis PEMS system in Fig. 1:

1) F is a nonlinear function with h and I as,

$$F = F_p + F_e = f_F(h, I), \quad (1)$$

where F has two components as,

- (i) Permanent magnetic force (F_p): F_p is the attractive magnetic force between the permanent magnet and the iron core of the electromagnet. And, F_p is a nonlinear decreasing function of h ¹⁹; and
- (ii) Electromagnetic force (F_e): F_e is the magnetic force between the permanent magnet and the electromagnet and is linear with I ⁸. As a sign conventional, $I > 0$ leads to attractive F_e , and vice versa.

2) U_h is a nonlinear function with h as,

$$U_h = f_h(h) \in (0, 3.3) \text{ V}. \quad (2)$$

Figure 3 visualizes the nonlinear characteristic of the ITR8307 distance sensor. It is observed that U_h is an increasing function of h with a decreasing slope.

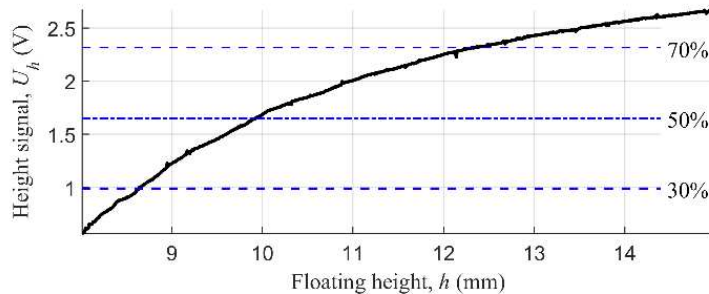


Figure 3. Nonlinear characteristic of the ITR8307 distance sensor.

3) I is a nonlinear function with $D \in (0,1)$ at a given f_{PWM} as,

$$I = f_I(D). \quad (3)$$

The present work aims to propose the suitable compensation algorithm by analyzing the nonlinear mechanism associated with the L298N full-bridge PWM inverter. Besides, f_F and f_h have been well acknowledged and compensated by various approaches, such as the gain scheduling method¹⁹.

Theoretical modelling

Figure 4 shows the electric circuit of the L298N full-bridge PWM inverter produced by STMicroelectronics. $In1$ and $In2$ are two TTL logic-level input ports and control the voltages at Nodes M and N, denoted as U_M and U_N , respectively. For example, $U_M \approx +U$ when $In1 = \text{HIGH}$, and $U_M \approx 0\text{ V}$ when $In1 = \text{LOW}$. Besides, the electromagnet can be modelled as a serial combination of an inductor (L) and a resistor (R). Denote the current in the electromagnet as i_{MN} and the voltage across as $u_{MN} = U_M - U_N$. Hence, the relationship between i_{MN} and u_{MN} can be expressed as,

$$u_{MN} = Ri_{MN} + L di_{MN}/dt, \quad (4)$$

where u_{MN} is driven by the full-bridge PWM inverter and i_{MN} varies continuously due to the inductor.

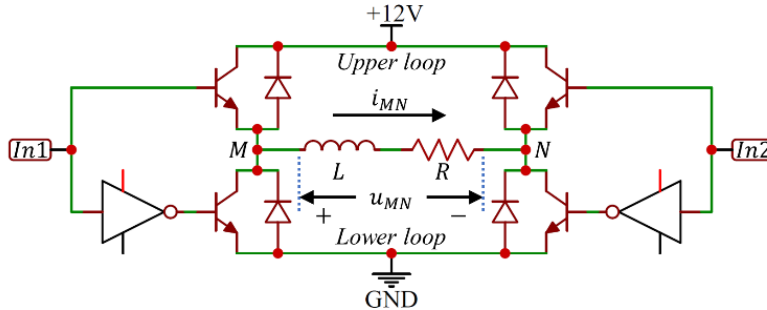


Figure 4. Electric circuit of L298N full-bridge PWM inverter.

Consequently, Table 2 lists out three modes of the full-bridge PWM inverter with the electromagnet. When $In1 \neq In2$, the electromagnet is either positively charged (+C) or negatively charged (-C) depending on the sign of u_{MN} ; when $In1 = In2$, the electromagnet is effectively short-circuited with $u_{MN} \approx 0\text{ V}$ and its magnetic energy is dissipated during the discharging (DC) mode. Meanwhile, in Table 3, four quadrants² are defined according to u_{MN} and i_{MN} . Generally, the energy flows from the power supply into the electromagnet ($|u_{MN}| < U$) during the forwards charging (FC) mode and flows from the electromagnet into the power supply ($|u_{MN}| > U$) during the backwards charging (BC) mode.

	$In1 = \text{HIGH}$	$In1 = \text{LOW}$
$In2 = \text{HIGH}$	DC: $u_{MN} \approx 0 V$.	-C: $u_{MN} \approx -U$.
$In2 = \text{LOW}$	+C: $u_{MN} \approx +U$.	DC: $u_{MN} \approx 0 V$.

Table 2. Three modes of full-bridge PWM inverter with electromagnet.

	$u_{MN} \approx -U$	$u_{MN} \approx +U$
$i_{MN} > 0$	(2nd quadrant) -BC: $u_{MN} < -U$.	(1st quadrant) +FC: $u_{MN} < +U$.
$i_{MN} < 0$	(3rd quadrant) -FC: $u_{MN} > -U$.	(4th quadrant) +BC: $u_{MN} > +U$.

Table 3. Four quadrants of full-bridge PWM inverter with electromagnet.

In the present work, $In1$ is the PWM signal generated by the STM32 controller and $In2$ is obtained by the NOT gate as,

$$In1 = PWM \text{ and } In2 = \overline{PWM}, \quad (5)$$

where the PWM signal can be explicitly expressed as,

$$PWM = \begin{cases} \text{HIGH}, & nT < t < (n+D)T \\ \text{LOW}, & (n+D)T < t < (n+1)T \end{cases} \quad (6)$$

where $T (= 1/f_{PWM})$ denotes the period of the PWM signal and n is any arbitrary integer.

Assuming the ideal full-bridge PWM inverter, u_{MN} can be expressed by referring to Table 2 and Eqs. (5-6) as,

$$u_{MN} = \begin{cases} +U, & nT < t < (n+D)T \\ -U, & (n+D)T < t < (n+1)T \end{cases} \quad (7)$$

Moreover, denote the equilibrium current at $t = nT$ as I_1 and that at $t = (n+D)T$ as I_2 . Solving Eq. (4) together with Eq. (7) gives the two equilibrium currents as,

$$\begin{cases} I_1 = \frac{U}{R} \left(e^{-\frac{RT}{L}} + 1 - 2e^{-\frac{(1-D)RT}{L}} \right) / \left(e^{-\frac{RT}{L}} - 1 \right) \\ I_2 = \frac{U}{R} \left(2e^{-\frac{DRT}{L}} - e^{-\frac{RT}{L}} - 1 \right) / \left(e^{-\frac{RT}{L}} - 1 \right) \end{cases}, \quad (8)$$

which indicates that i_{MN} fluctuates between I_1 and I_2 . Since the time constant of the electromagnet ($L/R \approx 5$ to 9 ms to be fully charged or discharged in Fig. 9) is much larger than the PWM period (e.g., $T = 0.1$ ms for 10 kHz), i.e., $RT/L \ll 1$, Eq. (8) can be approximated as,

$$i_{MN} \approx I_1 \approx I_2 \approx \frac{U}{R} (2D - 1) \in [-U/R, U/R], \quad (9)$$

which indicates that ideal i_{MN} in the electromagnet is linear with the duty cycle under a high f_{PWM} .

Nonlinear $i_{MN} - D$ characteristic

Figure 5(a) visualizes the variations of i_{MN} w.r.t. D for $f_{PWM} = 0.1, 1, 10, 100$ kHz. It is observed that the characteristic $i_{MN} - D$ function (f_I) is an odd function about Point (0.5, 0) as,

$$f_I(1 - D) = -f_I(D). \quad (10)$$

Also, the characteristic $i_{MN} - D$ curve deviates from the ideal line in Eq. (9), and the deviation increases with the increase of f_{PWM} .

Moreover, define the sensitivity of i_{MN} w.r.t. D as,

$$S = di_{MN}/dD. \quad (11)$$

Figure 5(b) visualizes the variations of S w.r.t. D . It is observed that S at $D = 0.5$ decreases with the increase of f_{PWM} (as low as 70 mA for 100 kHz), while the four sensitivity curves converge to around 1700 mA for $D < 0.3$ and $D > 0.7$.

Furthermore, since F is linear with i_{MN} ⁸, the large sensitivity change about the zero current (around 20 times for 100 kHz) will undermine the control stability of the zero-power PEMS system.

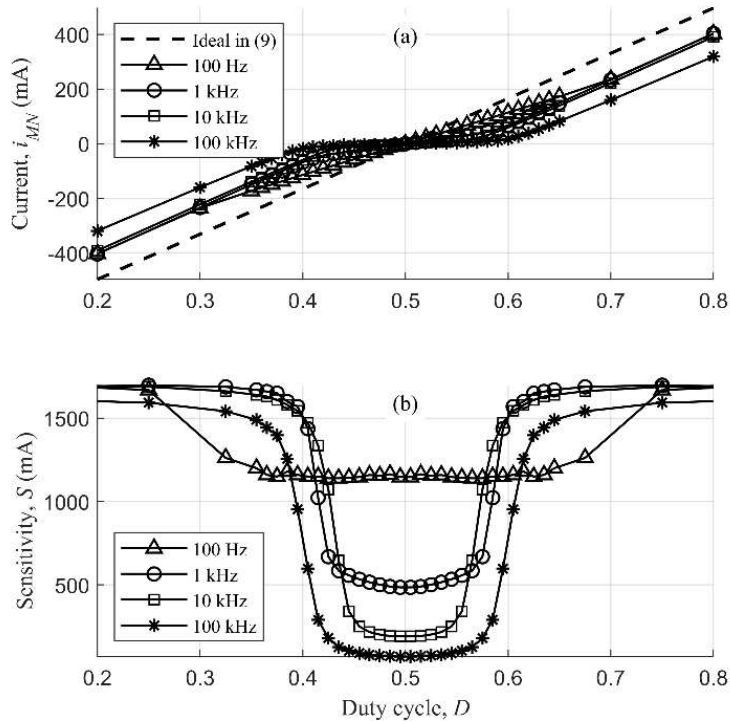


Figure 5. Variations of (a) i_{MN} and (b) S w.r.t. D for $f_{PWM} = 0.1, 1, 10, 100$ kHz.

Nonlinear Mechanism

This subsection analyzes the nonlinear $i_{MN} - D$ characteristic for the electromagnet driven by the L298N full-bridge PWM inverter. Firstly, into the voltage dynamics is investigated for $D = 0.5$ and two f_{PWM} , one

ultra-high and one ultra-low. Secondly, DC, FC and BC modes are respectively characterized. Thirdly, the critical PWM frequency (f_{cr}) is modeled from the energy perspective. Fourthly, the sensitivity transition is analyzed w.r.t. f_{cr} . Nevertheless, several remarks are addressed.

Voltage dynamics

- $f_{PWM} = 100$ kHz (ultra-high)

Figure 6 visualizes the whole-period variations of $In1$, $In2$, U_M , U_N , and u_{MN} for $f_{PWM} = 100$ kHz and $D = 0.5$ w.r.t. the time (t). It is observed that the dynamic responses of $In1$ and $In2$ are so fast that the step change is completed in less than $0.1 \mu\text{s}$, the rising and falling step changes of U_M and U_N are completed in $0.2 \mu\text{s}$ and $1 \mu\text{s}$, respectively. However, by comparing Figs. 6(a-b), there is a significant delay for around $2 \mu\text{s}$ between the falling step changes of U_M (or U_N) and $In1$ (or $In2$), which is referred to as the turn-off delay in the datasheet of IC L298N produced by STMicroelectronics. Therefore, the $2 \mu\text{s}$ turn-off delay results in the DC mode as defined in Table 2 and highlighted in Figure 6(c).

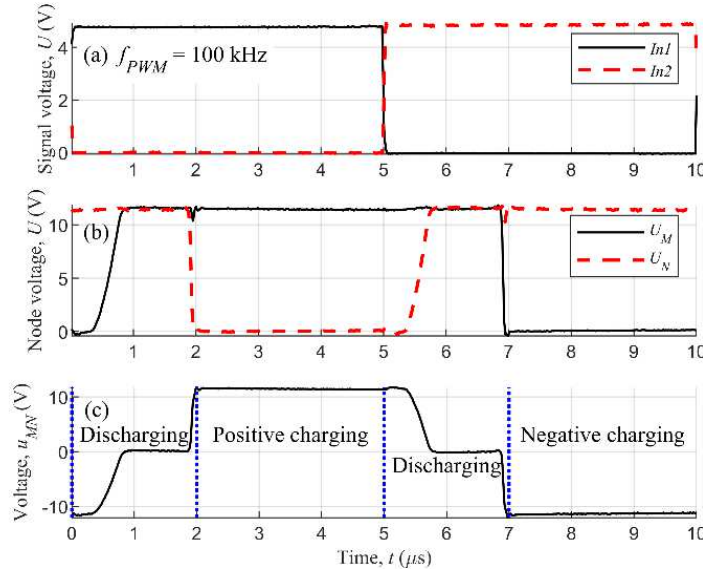


Figure 6. Whole-period variations of (a) $In1$ and $In2$, (b) U_M and U_N , and (c) u_{MN} for $f_{PWM} = 100$ kHz and $D = 0.5$ w.r.t. t . The $2 \mu\text{s}$ turn-off delay due to the IC L298N can be clearly observed for both U_M and U_N in (b). Three modes are highlighted in (c) according to u_{MN} .

- $f_{PWM} = 100$ Hz (ultra-low)

Figure 7 visualizes the whole-period variation of u_{MN} for $f_{PWM} = 100$ Hz and $D = 0.5$ w.r.t. t . Since the $2 \mu\text{s}$ turn-off delay is negligible compared with the 10 ms PWM period, the variations of $In1$, $In2$, U_M , and

U_N are trivial and not shown. As defined in Table 3, the BC and FC modes are separated by the boundaries at $u_{MN} = \pm 12 V$ in Fig. 7.

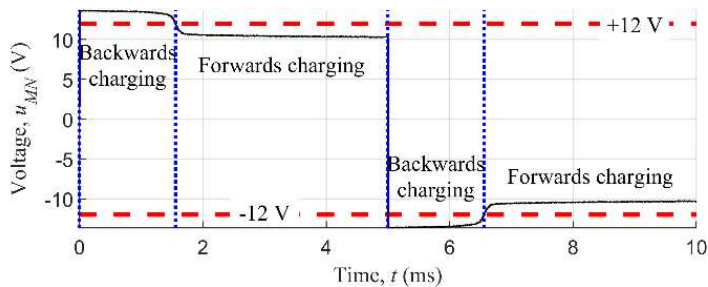


Figure 7. Whole-period variation of u_{MN} for $f_{PWM} = 100$ Hz and $D = 0.5$ w.r.t. t . The red dashed lines ($u_{MN} = \pm 12 V$) indicate the boundaries between the FC and BC modes.

Electronic characteristic

- Discharging characteristic

Figure 8 visualizes the step-change responses of u_{MN} in the initial $3 \mu s$ for $f_{PWM} = 5, 10, 20, 50,$ and 100 kHz and $D = 0.5$. It is observed that all five curves undergo the $2 \mu s$ DC mode. However, the BC mode ($u_{MN} > +12 V$) occurs immediately after the DC mode for $f_{PWM} = 5$ and 10 kHz, whereas the FC mode ($u_{MN} < +12 V$) occurs for $f_{PWM} = 20, 50,$ and 100 kHz.

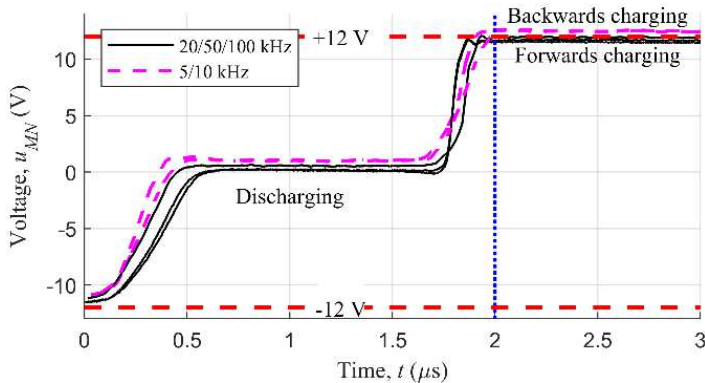


Figure 8. Initial-3- μs variations of u_{MN} w.r.t. t for $f_{PWM} = 5, 10, 20, 50,$ and 100 kHz and $D = 0.5$.

Technically, the energy-dissipation capability of the DC mode is finite in the $2 \mu s$ duration. Therefore, the immediate occurrence of the FC mode indicates that the magnetic energy is entirely dissipated by the DC mode for $f_{PWM} = 20, 50,$ and 100 kHz whereas the magnetic energy exceeds the energy-dissipation capability of the DC mode for $f_{PWM} = 5$ and 10 kHz.

- Charging characteristic

Figure 9 visualizes the step-change responses of u_{MN} in the initial 20 ms for $f_{PWM} = 2, 10, 20, 50, 100,$ and 200 Hz and $D = 0.5$. The six curves undergo the BC mode before the FC mode. Moreover, it is observed that the curves for $f_{PWM} = 2, 10,$ and 20 Hz have the longest BC mode for around 5 ms and the longest FC mode for around 9 ms, and fluctuate around $+10$ V afterwards. On the contrary, the curves for $f_{PWM} = 50, 100,$ and 200 Hz have shorter BC mode and falls out of the scope before reaching $+10$ V.

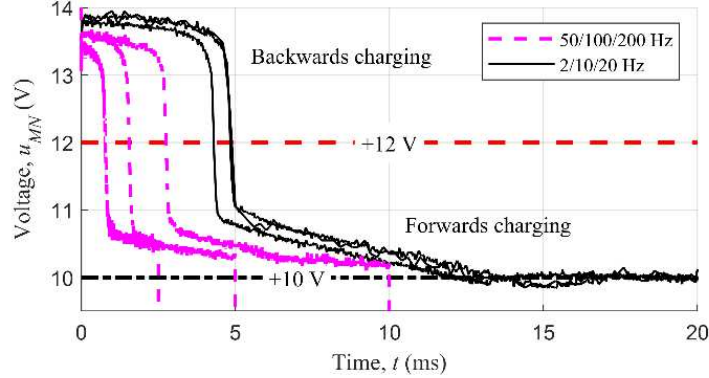


Figure 9. Initial-20-ms variations of u_{MN} w.r.t. t for $f_{PWM} = 2, 10, 20, 50, 100,$ and 200 Hz and $D = 0.5$.

Note that the 2 Hz and 10 Hz curves almost overlap with each other. The black dash-dot line ($u_{MN} = +10$ V) indicates the saturation of the FC mode.

Technically, the charging characteristic is determined by the power supply (e.g., supply voltage and inner resistance) and the electromagnet (e.g., inductance and resistance). Therefore, the saturation at $u_{MN} = \pm 10$ V indicates that the electromagnet is entirely charged by the FC mode for $f_{PWM} = 2, 10,$ and 20 Hz but is partially charged due to the insufficient duration for $f_{PWM} = 50, 100,$ and 200 Hz. Hence, $u_{MN} = \pm 9.5$ V can be regarded as the boundary between the DC mode and the two charging modes for the present experimental setup.

Critical PWM frequency

- Experimental observation

Figure 10 visualizes the contour of u_{MN} w.r.t. $\log_{10}(f_{PWM})$ and the normalized time (t/T) for $D = 0.5$. It is observed that the BC regime expands for $f_{PWM} \leq 100$ Hz, shrinks for $f_{PWM} > 100$ Hz, and vanishes at $f_{PWM} \approx 20$ kHz, whereas the DC regime expands exponentially. Besides, u_{MN} reaches the saturation at ± 10 V only for $f_{PWM} < 10^{1.5}$ Hz ≈ 31.6 Hz and is increasingly undercharged for $f_{PWM} > 31.6$ Hz.

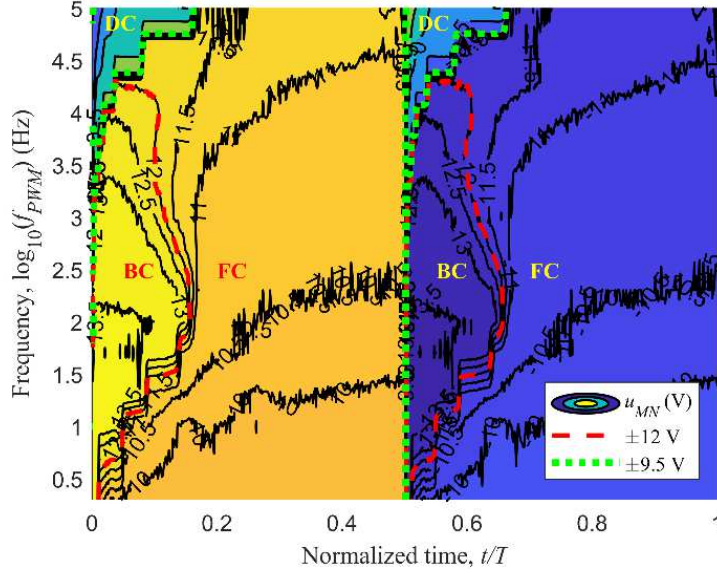


Figure 10. Contour of u_{MN} w.r.t. $\log_{10}(f_{PWM})$ and t/T for $D = 0.5$. The green dotted curves ($u_{MN} = \pm 9.5$ V) indicate the boundaries between the DC mode and the two charging modes.

Moreover, Table 4 lists out the relative portions of the three modes for various f_{PWM} and $D = 0.5$. Note that T_{FC} , T_{BC} , and T_{DC} ($= 2 \mu\text{s}$) denote durations of FC, BC, and DC modes, respectively.

f_{PWM} (kHz)	1	2	5	10	20	50	100
T_{BC}/T (%)	11.23	9.33	8.08	6.85	0.00	0.00	0.00
T_{DC}/T (%)	0.40	0.80	2.00	4.00	8.00	20.00	40.00
T_{FC}/T (%)	88.37	89.87	89.92	89.15	92.00	80.00	60.00

Table 4. Relative portions of three modes for various f_{PWM} and $D = 0.5$.

- Theoretical analysis

For $D = 0.5$, The magnetic energy (E) in the electromagnet is charged by the FC mode and dissipated by the DC and BC modes. And, the energy balance equation can be expressed as,

$$E_{FC} = E_{DC} + E_{BC}, \quad (12)$$

where E_{FC} , E_{DC} , and E_{BC} denote the charged energy by the FC mode and the dissipated energies by the DC and BC modes, respectively.

Moreover, assuming $T \ll L/R$, E_{FC} , E_{DC} , and E_{BC} can be linearized and approximated as,

$$E_{FC} = e_{FC}T_{FC}, E_{DC} = e_{DC}T_{DC}, E_{BC} = e_{BC}T_{BC}, \quad (13)$$

where e_{FC} , e_{DC} , and e_{BC} denote the energy-charging rate by the FC mode, and the energy-dissipating rates by the DC and BC modes, respectively.

Assuming $T_{DC} > 0$, substituting Eq. (13) into Eq. (12) gives,

$$T_{FC}/T_{DC} = (e_{BC}/e_{FC})(T_{BC}/T_{DC}) + e_{DC}/e_{FC}, \quad (14)$$

which is in the first-order form, i.e., $y = ax + b$, where $y = T_{FC}/T_{DC}$, $x = T_{BC}/T_{DC}$, $a = e_{BC}/e_{FC}$, and $b = e_{DC}/e_{FC}$. By substituting (x, y) associated with $f_{PWM} = 1, 2, 5,$ and 10 kHz in Table 4 into Eq. (14), (a, b) can be solved by the least square method as,

$$a = e_{BC}/e_{FC} = 7.46 \text{ and } b = e_{DC}/e_{FC} = 15.33, \quad (15)$$

which indicates that the energy-dissipating rate by the DC mode is around twice as much as that by the BC mode. Therefore, the DC mode gradually replaces the BC mode with the increase of f_{PWM} . Table 5 lists out the estimated relative portions of the three modes by Eq. (14) and the associated fitting errors for $f_{PWM} = 1, 2, 5,$ and 10 kHz and $D = 0.5$. For example, the fitting error ($=0.18\%$) for $f_{PWM} = 1$ kHz is the difference between T_{BC}/T ($=11.23\%$) and estimated T_{BC}/T ($=11.05\%$). Hence, the first-order estimation for the magnetic energy is generally acceptable with the low fitting error.

Furthermore, f_{cr} is defined as the vanishing point of the BC regime ($T_{BC} = 0$) for $D = 0.5$. Hence, f_{cr} can be calculated from Eq. (14) as 15.28 kHz.

f_{PWM} (kHz)	1	2	5	10	$f_{cr} = 15.28$	50
Estimated T_{BC}/T (%)	11.05	10.28	7.96	4.10	0.00	0.00
Estimated T_{DC}/T (%)	0.40	0.80	2.00	4.00	6.13	20.00
Estimated T_{FC}/T (%)	88.55	88.92	90.04	91.90	93.87	80.00
Fitting error (%)	0.18	-0.95	0.12	2.75	-	-

Table 5. Estimated relative portions of three modes and associated fitting errors for various f_{PWM} and $D = 0.5$.

Sensitivity transition

- Experimental observation

Figures 11(a-c) visualize the phase diagrams of u_{MN} w.r.t. D and t/T for $f_{PWM} = 1, 10,$ and 100 kHz. For $f_{PWM} = 1$ kHz, the boundaries between the FC and BC regimes are almost continuous as a result of the negligible DC regime; on the contrary, for $f_{PWM} = 100$ kHz, the BC regime is heavily squeezed by the DC regime. Besides, the cyan dotted lines indicate the termination points of the FC regimes.

Moreover, Figures 11(d-f) visualize the associated variations of S . The purple dotted lines indicate the transition points with $S = 1000$ mA. It is observed that the three sensitivity curves converge to the high sensitivity outside the purple dotted lines; the three curves stay near the respective minimum values between the cyan dotted lines; meanwhile, the sensitivity transitions take place between the purple and cyan dotted lines.

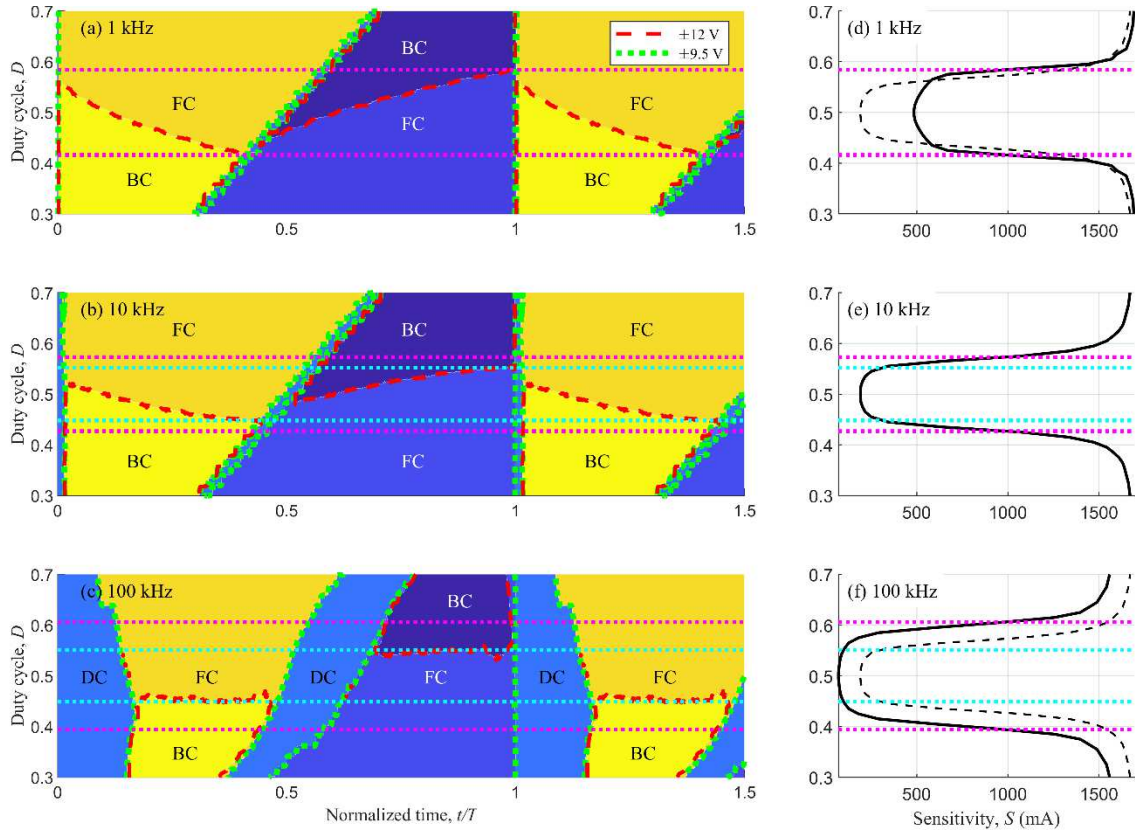


Figure 11. (a-c) Phase diagrams of u_{MN} w.r.t. D and t/T , and (d-f) variations of S w.r.t. D for $f_{PWM} = 1, 10,$ and 100 kHz. The cyan dotted lines indicate the termination points of the FC regimes, whereas the purple dotted lines indicate the transition points with $S = 1000$ mA. The dashed curve in (d&f) is the benchmark curve with $f_{PWM} = 10$ kHz.

- Theoretical analysis

Based on Fig. 11, Tables 6-7 outline the evolution of the three modes w.r.t. $D \geq 0.5$ for $f_{PWM} < f_{cr}$ and $f_{PWM} > f_{cr}$, respectively. The ‘+’ sign indicates $u_{MN} > 0$ and $di_{MN}/dt > 0$, while the ‘-’ sign indicates $u_{MN} < 0$ and $di_{MN}/dt < 0$. Also, the red background indicates $i_{MN} > 0$, the blue background indicates $i_{MN} < 0$, and the green background indicates $i_{MN} \approx 0$.

By referring to Tables 6-7, the variations of S can be characterized into three zones from the energy perspective:

- (i) **Low-sensitivity zone** (Stages I, II, and III, between the cyan dotted lines): Both +FC and -FC modes co-exist, which indicates that the magnetic energy stored during the FC mode (both positive and negative) is completely dissipated by the DC or BC mode. Therefore, the low-sensitivity zone is dominated by the energy cancellation between the FC and BC modes for $f_{PWM} < f_{cr}$ and between the FC and DC modes for $f_{PWM} > f_{cr}$.

(ii) **Sensitivity-transition zone** (Stage IV, between the purple and cyan dotted lines): The $2 \mu\text{s}$ DC mode has a finite energy-dissipation capability and buffers the sensitivity transition until the capability is entirely consumed, as outlined by the purple and cyan dotted lines. Therefore, the sensitivity transition expands with the increase of f_{PWM} .

(iii) **High-sensitivity zone** (Stage V, outside the purple dotted lines): The expanding of the FC regime and the shrinking of the BC regime occur simultaneously with the increase of the duty cycle. Therefore, the magnetic energy accumulates more effectively in the high-sensitivity zone than that in the low-sensitivity zone.

Stage	DT			$(1 - D)T$			Zone
V	-DC	+FC		-DC	-BC		High sensitivity
IV	DC	+FC		-DC	-BC		Sensitivity transition
III	DC	+FC		-DC	-BC	-FC	Low sensitivity
II	+DC	+FC		-DC	-BC	-FC	
I ($D \approx 0.5$)	+DC	+BC	+FC	-DC	-BC	-FC	

Table 6. Evolution of three modes w.r.t. $D \geq 0.5$ for $f_{PWM} < f_{cr}$.

Stage	DT			$(1 - D)T$			Zone
V	-DC	+FC		-DC	-BC		High sensitivity
IV	DC	+FC		-DC	-BC		Sensitivity transition
III	DC	+FC		-DC	-BC	-FC	Low sensitivity
II	DC	+FC		-DC	-FC		
I ($D \approx 0.5$)	DC	+FC	DC	-DC	-FC		

Table 7. Evolution of three modes w.r.t. $D \geq 0.5$ for $f_{PWM} > f_{cr}$.

Remarks

This subsection investigates into the nonlinear mechanism of the $i_{MN} - D$ characteristic. The experimental results indicate the following remarks:

- 1) In micro level, it is observed that the IC L298N possesses a $2 \mu\text{s}$ turn-off delay that leads to the passive DC mode; in macro level, such a tiny delay results in the nonlinear $i_{MN} - D$ characteristic.
- 2) With the increase of f_{PWM} , the relative portion of the $2 \mu\text{s}$ DC mode is significantly amplified and replaces the BC mode entirely at $D = 0.5$ and $f_{cr} = 15.28 \text{ kHz}$, which is theoretically modelled from the energy perspective.
- 3) The low-sensitivity zone is dominated by the energy cancellation between the FC and BC modes for $f_{PWM} < f_{cr}$ and by the energy cancellation between the FC mode and the $2 \mu\text{s}$ DC mode for $f_{PWM} > f_{cr}$.

4) The sensitivity transition results from the finite energy-dissipation capability of the 2 μ s DC mode and expands with the increase of f_{PWM} .

5) Though higher f_{PWM} can enhance the dynamic performance of the high-speed PEMS transportation system¹⁵, suitable compensation algorithm is necessary to take care of the nonlinear $i_{MN} - D$ characteristic especially for $f_{PWM} > f_{cr}$.

Compensation algorithm

Since F is linear with i_{MN} ⁸, this subsection proposes two piecewise linearization approaches to approximate the nonlinear $i_{MN} - D$ characteristic with the full-bridge PWM inverter. The compensation algorithm is verified by the current-step-change test over the sensitivity transition under two f_{PWM} w.r.t. f_{cr} .

For $f_{PWM} = 10 \text{ kHz} < f_{cr}$

- Piecewise Linearization

Figure 12(a) visualizes the nonlinear $i_{MN} - D$ characteristic for $f_{PWM} = 10 \text{ kHz} < f_{cr}$ together with three asymptotic lines. Asymptotic Line 1 is obtained by the two points at $D = 0.50$ and 0.51 , Asymptotic Line 2 is obtained by the two points at $D = 0.65$ and 0.70 , while Asymptotic Line 3 is obtained by the two points at $D = 0.57$ and 0.58 . The numerical expressions of the three asymptotic lines are,

$$\begin{cases} i_{MN}^{(1)} = f_I^{(1)}(D) = 200.1D - 100.1 \\ i_{MN}^{(2)} = f_I^{(2)}(D) = 1687.9D - 958.5. \\ i_{MN}^{(3)} = f_I^{(3)}(D) = 1072.0D - 590.6 \end{cases} \quad (16)$$

Note that the sensitivity ratio between $f_I^{(1)}$ and $f_I^{(2)}$ is more than 8 times, which will undermine the control stability of the single-axis PEMS system over the medium sensitivity transition of the nonlinear $i_{MN} - D$ characteristic. Besides, the three intersection points among the three asymptotic lines are highlighted in Fig. 12(a), including $A = (0.5770, 15.36 \text{ mA})$, $B = (0.5626, 12.48 \text{ mA})$, and $C = (0.5974, 49.77 \text{ mA})$.

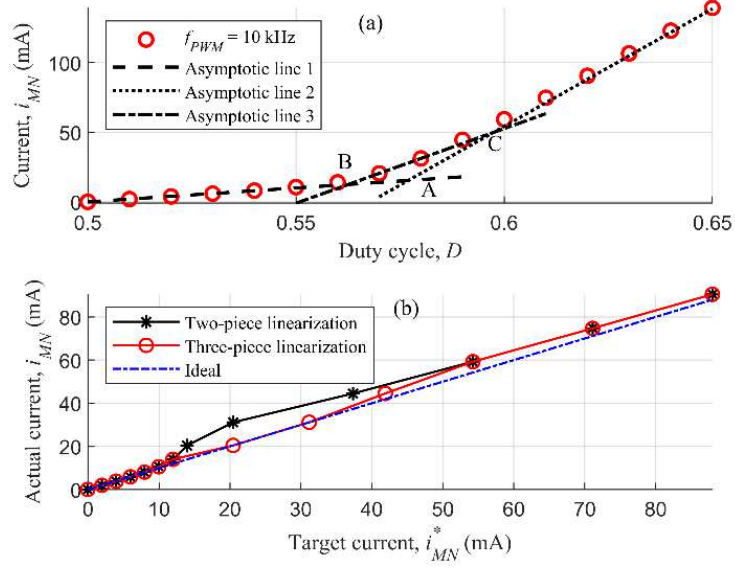


Figure 12. Variation of i_{MN} for $f_{PWM} = 10$ kHz w.r.t. (a) D together with three asymptotic lines, and (b) i_{MN}^* for the two piecewise linearization approaches.

Practically, the control algorithm generates the target current (i_{MN}^*), the compensation algorithm solves for the suitable duty cycle according to the piecewise linearization approach, and the real current (i_{MN}) is obtained in the electromagnet driven by the full-bridge PWM inverter. Hence, the two-piece linearization approach consists of Asymptotic Lines 1 and 2 as,

$$D = g_2(i_{MN}^*) = \begin{cases} (i_{MN}^* + 958.5)/1687.9, & i_{MN}^* > 15.36 \\ (i_{MN}^* + 100.1)/200.1, & -15.36 < i_{MN}^* < 15.36. \\ (i_{MN}^* + 729.4)/1687.9, & i_{MN}^* < -15.36 \end{cases} \quad (17)$$

And, the three-piece linearization approach consists of the three asymptotic lines as,

$$D = g_3(i_{MN}^*) = \begin{cases} (i_{MN}^* + 958.5)/1687.9, & i_{MN}^* > 49.77 \\ (i_{MN}^* + 590.6)/1072.0, & 12.48 < i_{MN}^* < 49.77 \\ (i_{MN}^* + 100.1)/200.1, & -12.48 < i_{MN}^* < 12.48 \\ (i_{MN}^* + 481.4)/1072.0, & -49.77 < i_{MN}^* < -12.48 \\ (i_{MN}^* + 729.4)/1687.9, & i_{MN}^* < -49.77 \end{cases} \quad (18)$$

Moreover, Figure 12(b) visualizes the $i_{MN} - i_{MN}^*$ curves by the two linearization approaches for $f_{PWM} = 10$ kHz. The maximum fitting errors are 34.3% and 14.4% by the two-piece linearization approach and the three-piece counterpart, respectively.

- Current-step-change test

As detailed in Sec A2, the single-axis PEMS system adopts the double-loop control algorithm embedded in the STM32 controller. In order to compare the two piecewise linearization approaches, the setpoint of the target current undergoes the following step changes as,

$$i_{MN}^{sp} = \begin{cases} 0 \text{ mA}, & t < 0 \text{ s} \\ -70 \text{ mA}, & 0 \leq t < 5 \text{ s} \\ 70 \text{ mA}, & 5 \leq t < 10 \text{ s} \\ 0 \text{ mA}, & t \geq 10 \text{ s} \end{cases} \quad (19)$$

Figure 13 visualizes the experimental results (U_h , i_{MN}^* , and D) under the current-step-change test with the two piecewise linearization approaches for $f_{PWM} = 10 \text{ kHz} < f_{cr}$. In order to remove the random noise, the averaged value is obtained from the ten consecutive repeats. From Figs. 13(b&e), it is observed that i_{MN}^* with noise varies within $\pm 10 \text{ mA}$ and averaged i_{MN}^* varies within $\pm 2 \text{ mA}$ for $t \geq 15 \text{ s}$. Therefore, the proposed compensation algorithm successfully achieved the zero-power PEMS system with the full-bridge PWM inverter.

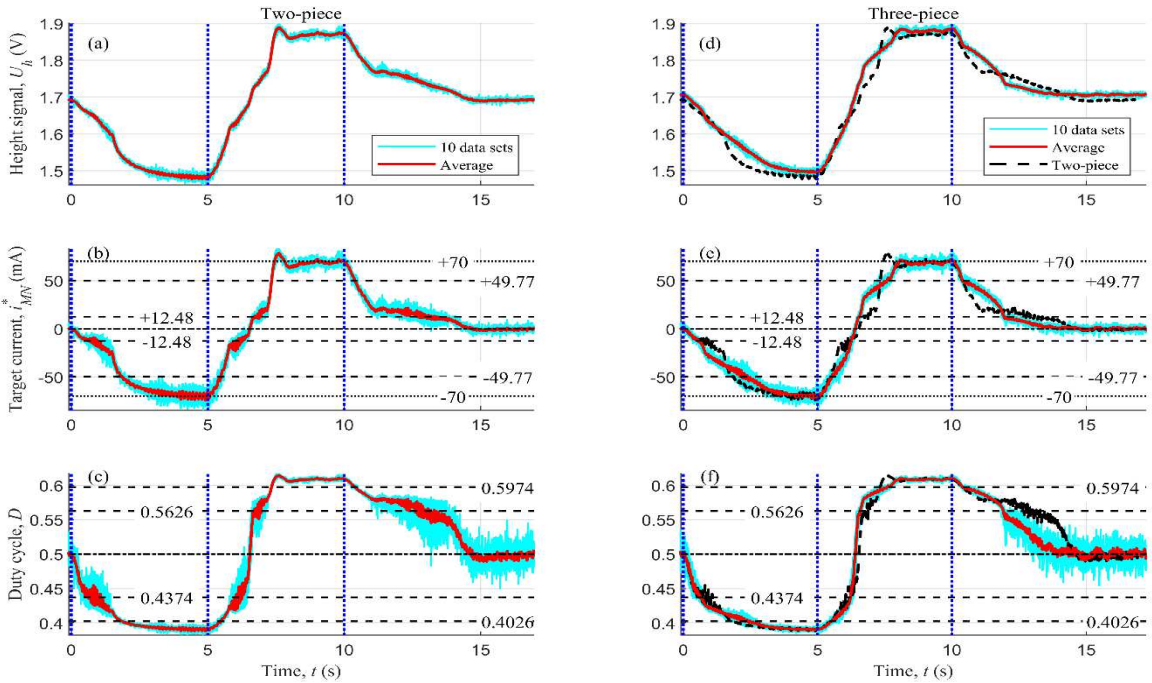


Figure 13. Experimental results of (a&d) U_h , (b&e) i_{MN}^* , and (c&f) D under the current-step-change test for $f_{PWM} = 10 \text{ kHz}$. The two columns correspond to the two-piece and three-piece linearization approaches, respectively. The cyan curves visualize ten repeats of the current-step-change test, whereas the red curves visualize the averaged value of the ten repeats. Intersection Points B and C, i.e., $(0.4374, -12.48 \text{ mA})$, $(0.5626, 12.48 \text{ mA})$, $(0.4026, -49.77 \text{ mA})$, and $(0.5974, 49.77 \text{ mA})$, are highlighted by horizontal black dashed lines.

Moreover, in Figs. 13(a&d), U_h vary between 1.46 V and 1.90 V during the current-step-change test. By referring to Fig. 3, h fluctuates within 1.5 mm, which is a close neighborhood of the equilibrium point. Hence, the single-axis PEMS system keeps stable with the unchanged control parameters throughout the current-step-change test. Note that the high noise level for $D \in [0.4374, 0.5626]$ in Figs. 13(c&f) results from the smaller sensitivity of Asymptotic Line 1.

Nevertheless, Figures 13(d-f) compare the two piecewise linearization approaches by the averaged results (U_h , i_{MN}^* , and D). In Figs. 13(d-e), U_h and i_{MN}^* with the two-piece linearization approach significantly overshoot around $t = 7.5$ s, when bypassing Intersection Point C (0.5974, 49.77 mA). Meanwhile, in Fig. 13(f), D with the two-piece linearization approach significantly deviates from that with the three-piece counterpart around $t = 13.0$ s when bypassing Intersection Point B (0.5626, 12.48 mA). Therefore, the three-piece linearization approach outperforms the two-piece linearization approach with stronger robustness and smoother dynamics under the current-step-change test over the medium sensitivity transition for $f_{PWM} = 10 \text{ kHz} < f_{cr}$.

For $f_{PWM} = 50 \text{ kHz} > f_{cr}$

- Piecewise Linearization

Figure 14(a) visualizes the nonlinear $i_{MN} - D$ characteristic for $f_{PWM} = 50 \text{ kHz} > f_{cr}$ together with three asymptotic lines. Asymptotic Line 1 is obtained by the two points at $D = 0.50$ and 0.51 , Asymptotic Line 2 is obtained by the two points at $D = 0.65$ and 0.70 , while Asymptotic Line 3 is obtained by the three points at $D = 0.57, 0.58$ and 0.59 . The numerical expressions of the three asymptotic lines are,

$$\begin{cases} i_{MN}^{(1)} = f_I^{(1)}(D) = 92.5D - 46.1 \\ i_{MN}^{(2)} = f_I^{(2)}(D) = 1654.8D - 962.6. \\ i_{MN}^{(3)} = f_I^{(3)}(D) = 615.5D - 341.6 \end{cases} \quad (20)$$

Note that the sensitivity ratio between $f_I^{(1)}$ and $f_I^{(2)}$ is around 18 times, which will severely undermine the control stability of the single-axis PEMS system over the harsh sensitivity transition of the nonlinear $i_{MN} - D$ characteristic. Besides, the three intersection points among the three asymptotic lines are highlighted in Fig. 14(a), including $A = (0.5867, 8.18 \text{ mA})$, $B = (0.5650, 6.18 \text{ mA})$, and $C = (0.5975, 26.18 \text{ mA})$.

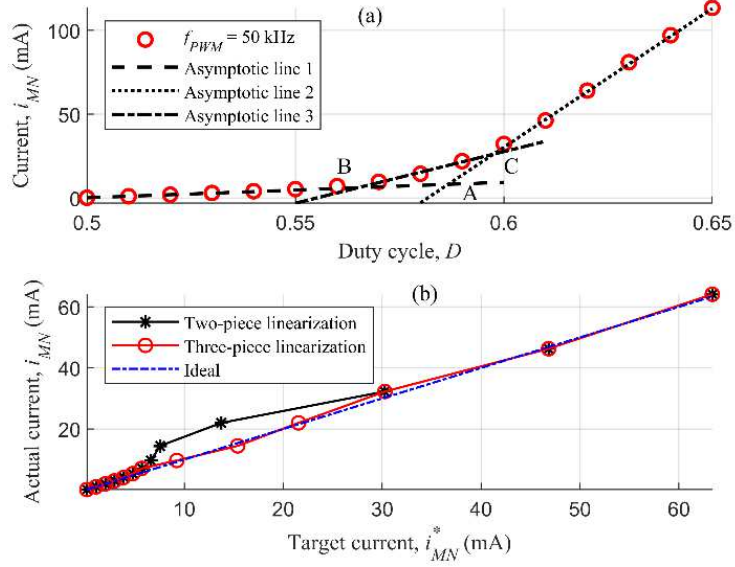


Figure 14. Variation of i_{MN} for $f_{PWM} = 50$ kHz w.r.t. (a) D together with three asymptotic lines, and (b) i_{MN}^* for the two piecewise linearization approaches.

Hence, the two-piece linearization approach consists of Asymptotic Lines 1 and 2 as,

$$D = g_2(i_{MN}^*) = \begin{cases} (i_{MN}^* + 962.6)/1654.8, & i_{MN}^* > 8.18 \\ (i_{MN}^* + 46.1)/92.5, & -8.18 < i_{MN}^* < 8.18. \\ (i_{MN}^* + 692.2)/1654.8, & i_{MN}^* < -8.18 \end{cases} \quad (21)$$

And, the three-piece linearization approach consists of the three asymptotic lines as,

$$D = g_3(i_{MN}^*) = \begin{cases} (i_{MN}^* + 962.6)/1654.8, & i_{MN}^* > 26.18 \\ (i_{MN}^* + 341.6)/615.5, & 6.18 < i_{MN}^* < 26.18 \\ (i_{MN}^* + 46.1)/92.5, & -6.18 < i_{MN}^* < 6.18 \\ (i_{MN}^* + 273.9)/615.5, & -26.18 < i_{MN}^* < -6.18 \\ (i_{MN}^* + 692.2)/1654.8, & i_{MN}^* < -26.18 \end{cases} \quad (22)$$

Moreover, Figure 14(b) visualizes the $i_{MN} - i_{MN}^*$ curves by the two linearization approaches for $f_{PWM} = 50$ kHz. The maximum fitting errors are 47.8% and 19.6% by the two-piece linearization approach and the three-piece counterpart, respectively.

- Current-step-change test

Figure 15 visualizes the experimental results (U_h , i_{MN}^* , and D) under the current-step-change test with the two piecewise linearization approaches for $f_{PWM} = 50$ kHz $> f_{cr}$. From Figs. 15(b&e), it is observed that i_{MN}^* with noise varies within ± 6 mA and averaged i_{MN}^* varies within ± 2 mA for $t \geq 15$ s.

Moreover, Figures 15(d-f) compare the two piecewise linearization approaches by the averaged results (U_h , i_{MN}^* , and D). In Figs. 15(d-e), U_h and i_{MN}^* with the two-piece linearization approach significantly

overshoot around $t = 1, 7,$ and 11 s, when bypassing Intersection Point C, $(0.4025, -26.18$ mA) and $(0.5975, 26.18$ mA). Meanwhile, in Fig. 15(f), D with the two-piece linearization approach significantly deviates from that with the three-piece counterpart around $t = 13.0$ s when bypassing Intersection Point B $(0.5650, 6.18$ mA). Therefore, the three-piece linearization approach greatly outperforms the two-piece linearization approach with stronger robustness and smoother dynamics under the current-step-change test over the harsh sensitivity transition for $f_{PWM} = 50$ kHz $>$ f_{cr} .

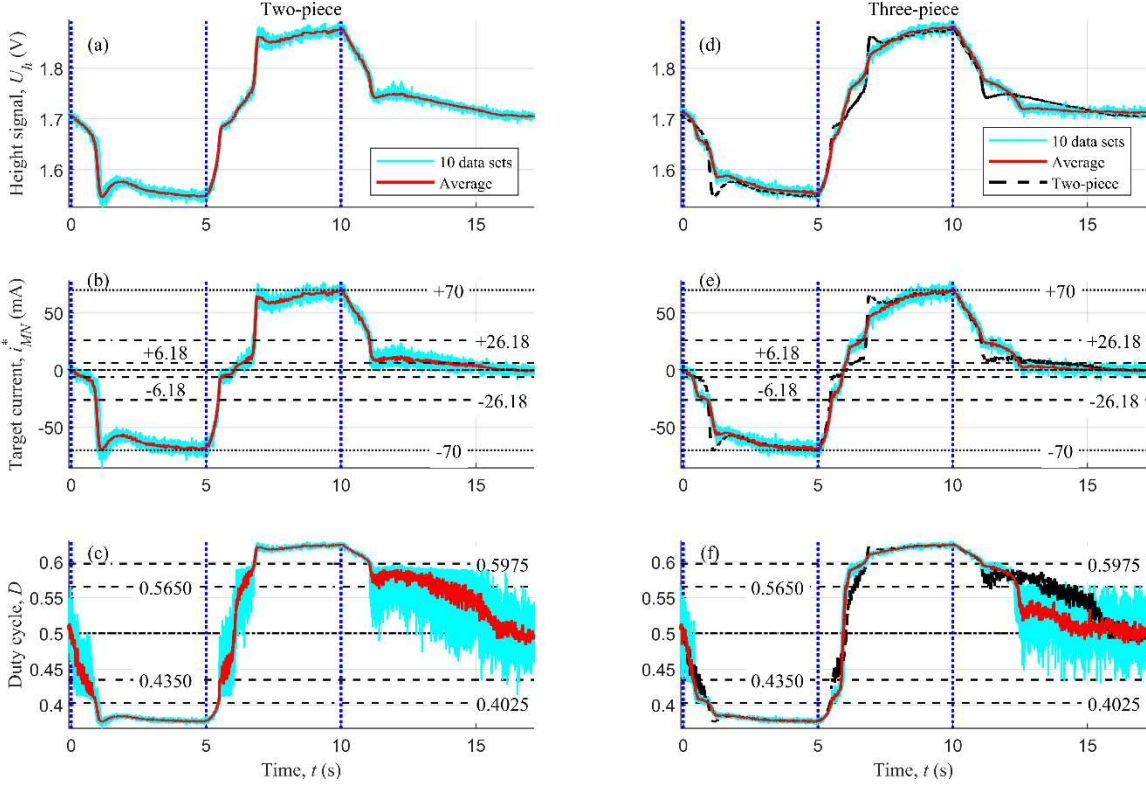


Figure 15. Experimental results of (a&d) U_h , (b&e) i_{MN}^* , and (c&f) D under the current-step-change test for $f_{PWM} = 50$ kHz. The two columns correspond to the two-piece and three-piece linearization approaches, respectively. The cyan curves visualize ten repeats of the current-step-change test, whereas the red curves visualize the averaged value of the ten repeats. Intersection Points B and C, i.e., $(0.4350, -6.18$ mA), $(0.5650, 6.18$ mA), $(0.4025, -26.18$ mA), and $(0.5975, 26.18$ mA), are highlighted by horizontal black dashed lines.

Remarks

This subsection verifies the proposed compensation algorithm for the L298N full-bridge PWM inverter in the zero-power PEMS system. The experimental results indicate the following remarks:

1) The piecewise linearization approach with more pieces can better approximate the sensitivity transition of the nonlinear $i_{MN} - D$ characteristic. Besides, other fitting approaches, e.g., polynomial fitting, can serve the same purpose as well.

2) Under the current-step-change test over the sensitivity transition, the three-piece linearization approach successfully stabilizes the single-axis PEMS system with only a few milliamper current and demonstrates stronger robustness and smoother dynamics than the two-piece counterpart especially for $f_{PWM} = 50 \text{ kHz} > f_{cr}$.

Discussion

The present work investigates into the nonlinear mechanism of the L298N full-bridge PWM inverter, proposes the compensation algorithm, and realizes for the zero-power PEMS system with record-breaking $f_{PWM} = 50 \text{ kHz}$. Based on the experimental observation and the theoretical analysis, we can draw the following conclusions:

1) **Nonlinear mechanism:** the $2 \mu\text{s}$ turn-off delay of the IC L298N leads to the DC mode that accounts for f_{cr} and the sensitivity transition.

2) **Compensation algorithm:** the piecewise linearization approach overcomes the sensitivity transition and stabilizes the zero-power PEMS system especially for $f_{PWM} > f_{cr}$. The lower fitting error, the stronger robustness and the smoother dynamics under the current-step-change test.

Therefore, in order to enhance the dynamic performance of the high-speed PEMS transportation, higher f_{PWM} can be realized by reducing (i) the turn-off delay of the full-bridge PWM inverter and (ii) the fitting error of the compensation algorithm.

Methods

Analog Signal Processor

Figure 16 visualizes the electric circuit of the analog signal processor. The height signal (U_h) is generated by the ITR8307 opto interrupter and processed by the LM324 operational amplifier for the proportional and derivative signals (U_p & U_d),

$$\begin{cases} U_p = (1.65 - U_h) R_{P2}/R_{P1} + 1.65 = 1.35(1.65 - U_h) + 1.65 \\ U_d = C_d R_D d(1.65 - U_h)/dt + 1.65 = -0.19 dU_h/dt + 1.65 \end{cases} \quad (23)$$

where U_p and U_d are the two inputs to the 12-bit analog-digital converters of the STM32 controller.

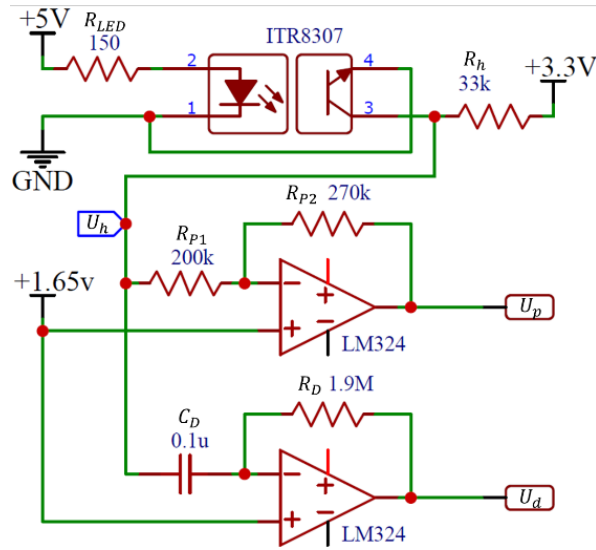


Figure 16. Electric circuit of the analog signal processor.

Digital STM32 Controller

Figure 17 visualizes the double-loop block diagram for the STM32 controller with $f_{sample} = 200$ Hz. The height loop involves two functional blocks, including the proportional-integral-derivative (PID) height controller (C_{height}) and the compensation algorithm ($g_{2\ or\ 3}$). The PID height controller adopts the incremental algorithm as,

$$\begin{aligned} \Delta i_{MN}^* &= i_{MN}^*[n] - i_{MN}^*[n-1] \\ &= k_{p,height}(U_p[n] - U_p[n-1]) + k_{i,height}(U_p[n] - U_p^{sp}[n]) \\ &\quad + k_{d,height}(U_d[n] - U_d[n-1]) \end{aligned} \quad (24)$$

where i_{MN}^* is the target current and U_p^{sp} is the setpoint of U_p . Then, D is calculated by the compensation algorithm, and the L298N full-bridge PWM inverter drives the electromagnet.

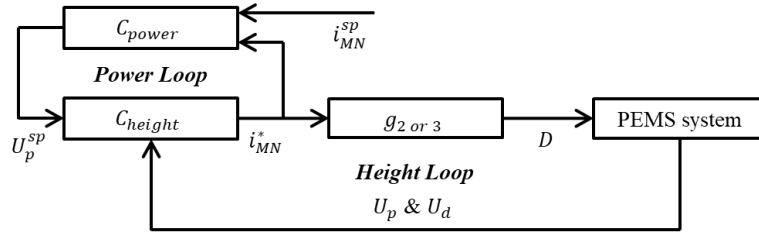


Figure 17. Double-loop block diagram for the STM32 controller.

Moreover, the power loop involves the integral power controller (C_{power}) to maintains the constant power by adjusting U_p^{sp} as,

$$\Delta U_p^{sp} = U_p^{sp}[n] - U_p^{sp}[n-1] = k_{i,power}(i_{MN}^*[n] - i_{MN}^{sp}[n]) \quad (25)$$

where i_{MN}^{sp} is the setpoint of the target current. For example, $i_{MN}^{sp} = 0$ results in the zero-power PEMS system.

Nevertheless, Table 8 lists out the four control parameters adopted in the present work.

Parameter	Value	Unit
$k_{p,height}$	376.36	mA/V
$k_{i,height}$	1.25	mA/V
$k_{d,height}$	75.27	mA/V
$k_{i,power}$	1.20×10^{-5}	V/mA

Table 8. Control parameters for stm32 controller.

References

- 1 Lee, H. W., Kim, K. C. & Lee, J. Review of maglev train technologies. *IEEE Transactions on Magnetics* **42**, 1917-1925, doi:10.1109/Tmag.2006.875842 (2006).
- 2 Schuhmann, T., Hofmann, W. & Werner, R. Improving operational performance of active magnetic bearings using kalman filter and state feedback control. *IEEE Transactions on Industrial Electronics* **59**, 821-829, doi:10.1109/TIE.2011.2161056 (2012).
- 3 Liu, Z. G., Long, Z. Q. & Li, X. L. *Maglev trains: key underlying technologies*. 1st edn, (Springer, 2015).
- 4 Zhang, Z., She, L., Zhang, L., Shang, C. & Chang, W. S. Structural optimal design of a permanent-electro magnetic suspension magnet for middle-low-speed maglev trains. *IET Electrical Systems in Transportation* **1**, 61-68, doi:10.1049/iet-est.2010.0018 (2011).
- 5 Feng, W., Lee, F. C. & Mattavelli, P. Simplified optimal trajectory control (SOTC) for LLC resonant converters. *IEEE Transactions on Power Electronics* **28**, 457-466, doi:10.1109/TPEL.2012.2200110 (2013).
- 6 Morishita, M. & Azukizawa, T. Zero power control of electromagnetic levitation system. *Electrical Engineering in Japan* **108**, 111-120, doi:10.1002/eej.4391080313 (1988).
- 7 Mizuno, T., Takasaki, M., Kishita, D. & Hirakawa, K. Vibration isolation system combining zero-power magnetic suspension with springs. *Control Engineering Practice* **15**, 187-196, doi:10.1016/j.conengprac.2006.06.001 (2007).
- 8 Zhang, Z. Y., Gao, T., Qin, Y., Yang, J. & Zhou, F. Z. Numerical study for zero-power maglev system inspired by undergraduate project kits. *IEEE Access* **8**, 90316-90323, doi:10.1109/access.2020.2994128 (2020).
- 9 Tzeng, Y. K. & Wang, T. C. Dynamic analysis of the maglev system using controlled-PM electromagnets and robust zero-power-control strategy. *IEEE Transactions on Magnetics* **31**, 4211-4213, doi:10.1109/20.489929 (1995).
- 10 Cho, S. Y., Kim, W. H., Jang, I. S., Kang, D. W. & Lee, J. Robust zero power levitation control of quadruple hybrid EMS system. *Journal of Electrical Engineering & Technology* **8**, 1451-1456, doi:10.5370/Jeet.2013.8.6.1451 (2013).
- 11 Zad, H. S., Khan, T. I. & Lazoglu, I. Design and adaptive sliding-mode control of hybrid magnetic bearings. *IEEE Transactions on Industrial Electronics* **65**, 2537-2547, doi:10.1109/tie.2017.2739682 (2017).
- 12 Lee, S. H., Sung, H. K., Lim, J. T. & Bien, Z. Self-tuning control of electromagnetic levitation systems. *Control Engineering Practice* **8**, 749-756, doi:10.1016/S0967-0661(00)00005-8 (2000).

- 13 Wai, R. J., Lee, J. D. & Chuang, K. L. Real-time PID control strategy for maglev transportation system via particle swarm optimization. *IEEE Transactions on Industrial Electronics* **58**, 629-646, doi:10.1109/Tie.2010.2046004 (2011).
- 14 Banerjee, S., Sarkar, M. K., Biswas, P. K., Bhaduri, R. & Sarkar, P. A review note on different components of simple electromagnetic levitation systems. *IETE Technical Review* **28**, 256-264, doi:10.4103/0256-4602.81241 (2011).
- 15 WANG, Z. Q., LONG, Z. Q. & LI, X. L. Track irregularity disturbance rejection for maglev train based on online optimization of PnP control architecture. *IEEE Access* **7**, 12610 - 12619, doi:10.1109/ACCESS.2019.2891964 (2019).
- 16 Carmichael, A. T., Hinchliffe, S., Murgatroyd, P. N. & Williams, I. D. Magnetic suspension systems with digital controllers. *Review of Scientific Instruments* **57**, 1611-1615, doi:10.1063/1.1138539 (1986).
- 17 Zhang, Y., Xian, B. & Ma, S. Continuous robust tracking control for magnetic levitation system with unidirectional input constraint. *IEEE Transactions on Industrial Electronics* **62**, 5971-5980, doi:10.1109/TIE.2015.2434791 (2015).
- 18 Mittal, S. & Menq, C. H. Precision motion control of a magnetic suspension actuator using a robust nonlinear compensation scheme. *IEEE/ASME Transactions on Mechatronics* **2**, 268-280, doi:10.1109/3516.653051 (1997).
- 19 Zhang, C., Lu, Y. H., Liu, G. C. & Ye, Z. B. Research on one-dimensional motion control system and method of a magnetic levitation ball. *Review of Scientific Instruments* **90**, 1-9, doi:10.1063/1.5119767 (2019).

Acknowledgements

This work was supported in part by the high-level talents research start-up project of Jiangxi University of Science and Technology under Grant 205200100476.

Author contributions statement

This is a single-author paper.

Additional information

Correspondence and requests for materials should be addressed to Z.Z.

Competing interests statement

The author(s) declare no competing interests.

Legends

Figure 1. Close-loop architecture of the single-axis PEMS system.

Figure 2. Hardware of the single-axis PEMS system, (a) stereoscopic view and (b) cross-sectional view for the electromagnet and the permanent magnet, (c) electronic devices, and (d) experiment rig.

Figure 3. Nonlinear characteristic of the ITR8307 distance sensor.

Figure 4. Electric circuit of L298N full-bridge PWM inverter.

Figure 5. Variations of (a) i_{MN} and (b) S w.r.t. D for $f_{PWM} = 0.1, 1, 10, 100$ kHz.

Figure 6. Whole-period variations of (a) $In1$ and $In2$, (b) U_M and U_N , and (c) u_{MN} for $f_{PWM} = 100$ kHz and $D = 0.5$ w.r.t. t . The $2\ \mu\text{s}$ turn-off delay due to the IC L298N can be clearly observed for both U_M and U_N in (b). Three modes are highlighted in (c) according to u_{MN} .

Figure 7. Whole-period variation of u_{MN} for $f_{PWM} = 100$ Hz and $D = 0.5$ w.r.t. t . The red dashed lines ($u_{MN} = \pm 12$ V) indicate the boundaries between the FC and BC modes.

Figure 8. Initial-3- μs variations of u_{MN} w.r.t. t for $f_{PWM} = 5, 10, 20, 50,$ and 100 kHz and $D = 0.5$.

Figure 9. Initial-20-ms variations of u_{MN} w.r.t. t for $f_{PWM} = 2, 10, 20, 50, 100,$ and 200 Hz and $D = 0.5$. Note that the 2 Hz and 10 Hz curves almost overlap with each other. The black dash-dot line ($u_{MN} = +10$ V) indicates the saturation of the FC mode.

Figure 10. Contour of u_{MN} w.r.t. $\log_{10}(f_{PWM})$ and t/T for $D = 0.5$. The green dotted curves ($u_{MN} = \pm 9.5$ V) indicate the boundaries between the DC mode and the two charging modes.

Figure 11. (a-c) Phase diagrams of u_{MN} w.r.t. D and t/T , and (d-f) variations of S w.r.t. D for $f_{PWM} = 1, 10,$ and 100 kHz. The cyan dotted lines indicate the termination points of the FC regimes, whereas the purple dotted lines indicate the transition points with $S = 1000$ mA. The dashed curve in (d&f) is the benchmark curve with $f_{PWM} = 10$ kHz.

Figure 12. Variation of i_{MN} for $f_{PWM} = 10$ kHz w.r.t. (a) D together with three asymptotic lines, and (b) i_{MN}^* for the two piecewise linearization approaches.

Figure 13. Experimental results of (a&d) U_h , (b&e) i_{MN}^* , and (c&f) D under the current-step-change test for $f_{PWM} = 10$ kHz. The two columns correspond to the two-piece and three-piece linearization approaches,

respectively. The cyan curves visualize ten repeats of the current-step-change test, whereas the red curves visualize the averaged value of the ten repeats. Intersection Points B and C, i.e., (0.4374, -12.48 mA), (0.5626, 12.48 mA), (0.4026, -49.77 mA), and (0.5974, 49.77 mA), are highlighted by horizontal black dashed lines.

Figure 14. Variation of i_{MN} for $f_{PWM} = 50$ kHz w.r.t. (a) D together with three asymptotic lines, and (b)

Figure 15. Experimental results of (a&d) U_h , (b&e) i_{MN}^* , and (c&f) D under the current-step-change test for $f_{PWM} = 50$ kHz. The two columns correspond to the two-piece and three-piece linearization approaches, respectively. The cyan curves visualize ten repeats of the current-step-change test, whereas the red curves visualize the averaged value of the ten repeats. Intersection Points B and C, i.e., (0.4350, -6.18 mA), (0.5650, 6.18 mA), (0.4025, -26.18 mA), and (0.5975, 26.18 mA), are highlighted by horizontal black dashed lines.

Figure 16. Electric circuit of the analog signal processor.

Figure 17. Double-loop block diagram for the STM32 controller.

Table 1. Physical properties of the single-axis PEMS system.

Table 2. Three modes of full-bridge PWM inverter with electromagnet.

Table 3. Four quadrants of full-bridge PWM inverter with electromagnet.

Table 4. Relative portions of three modes for various f_{PWM} and $D = 0.5$.

Table 5. Estimated relative portions of three modes and associated fitting errors for various f_{PWM} and $D = 0.5$.

Table 6. Evolution of three modes w.r.t. $D \geq 0.5$ for $f_{PWM} < f_{cr}$.

Table 7. Evolution of three modes w.r.t. $D \geq 0.5$ for $f_{PWM} > f_{cr}$.

Table 8. Control parameters for stm32 controller.

Figures

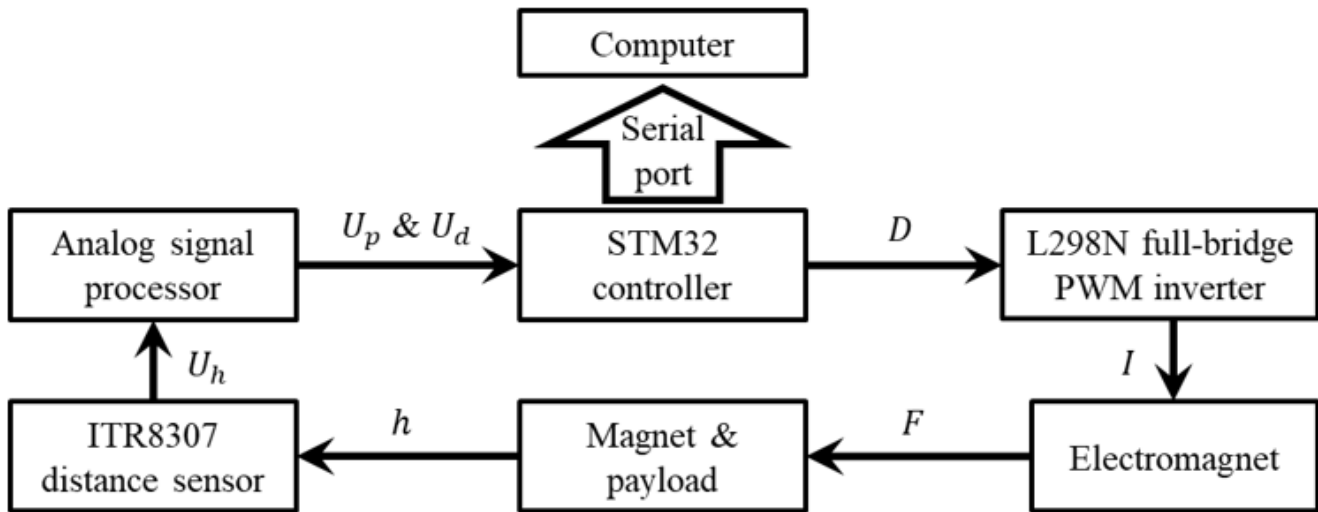


Figure 1

Close-loop architecture of the single-axis PEMS system.

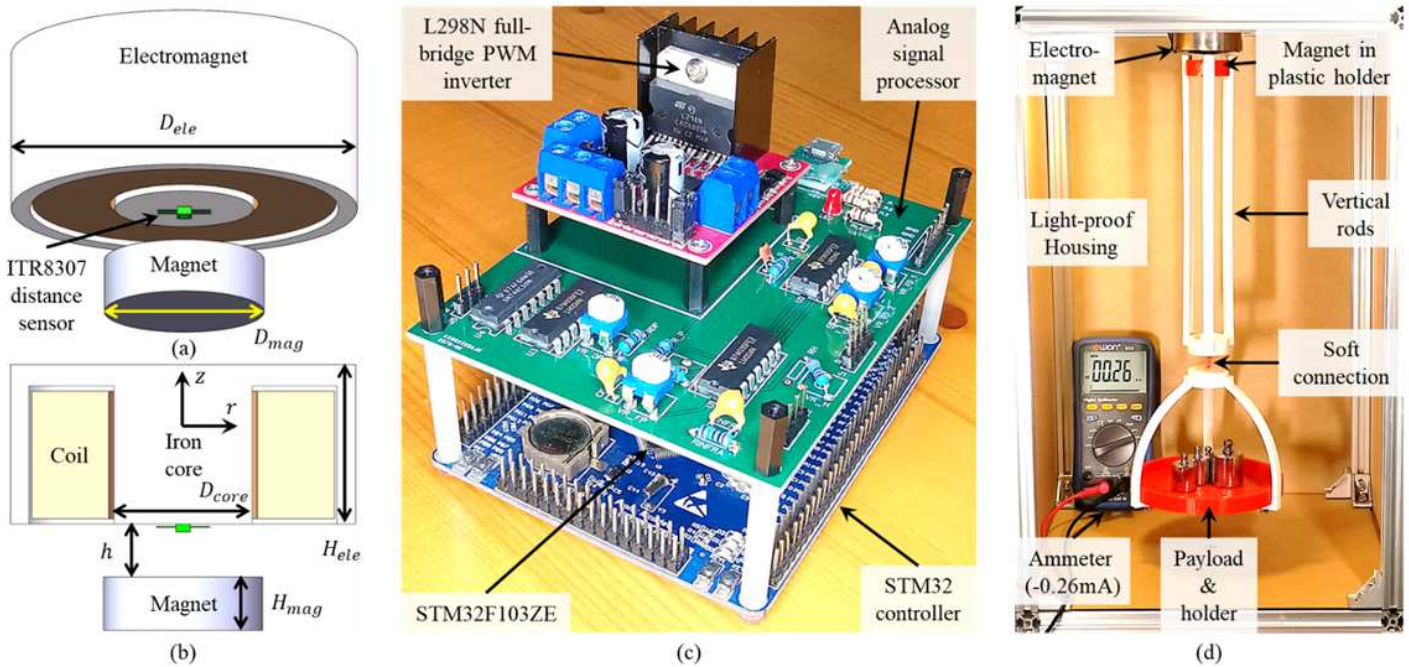


Figure 2

Hardware of the single-axis PEMS system, (a) stereoscopic view and (b) cross-sectional view for the electromagnet and the permanent magnet, (c) electronic devices, and (d) experiment rig.

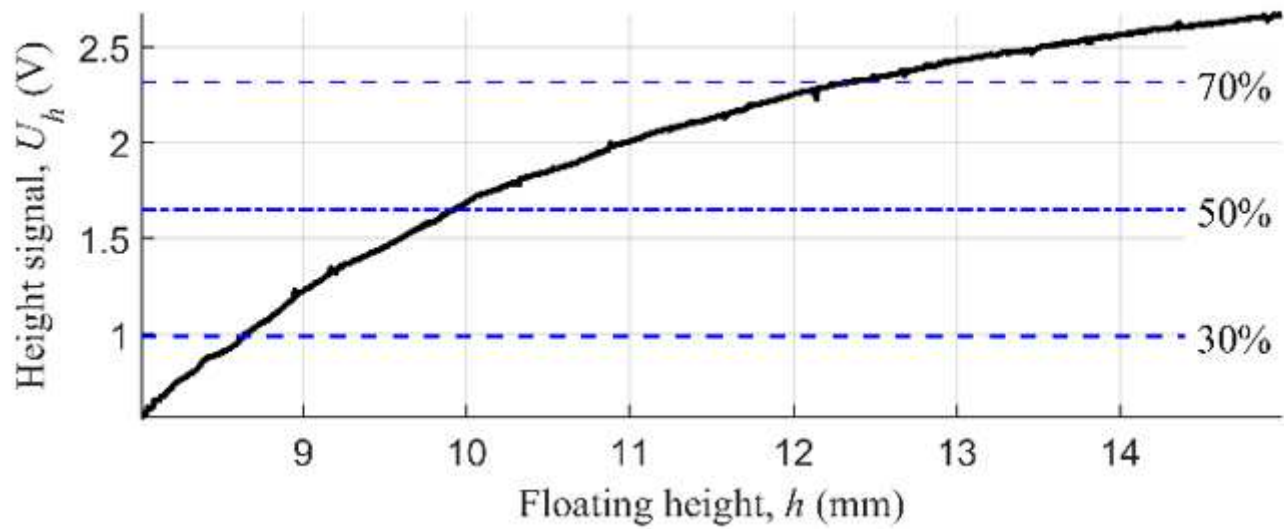


Figure 3

Nonlinear characteristic of the ITR8307 distance sensor.

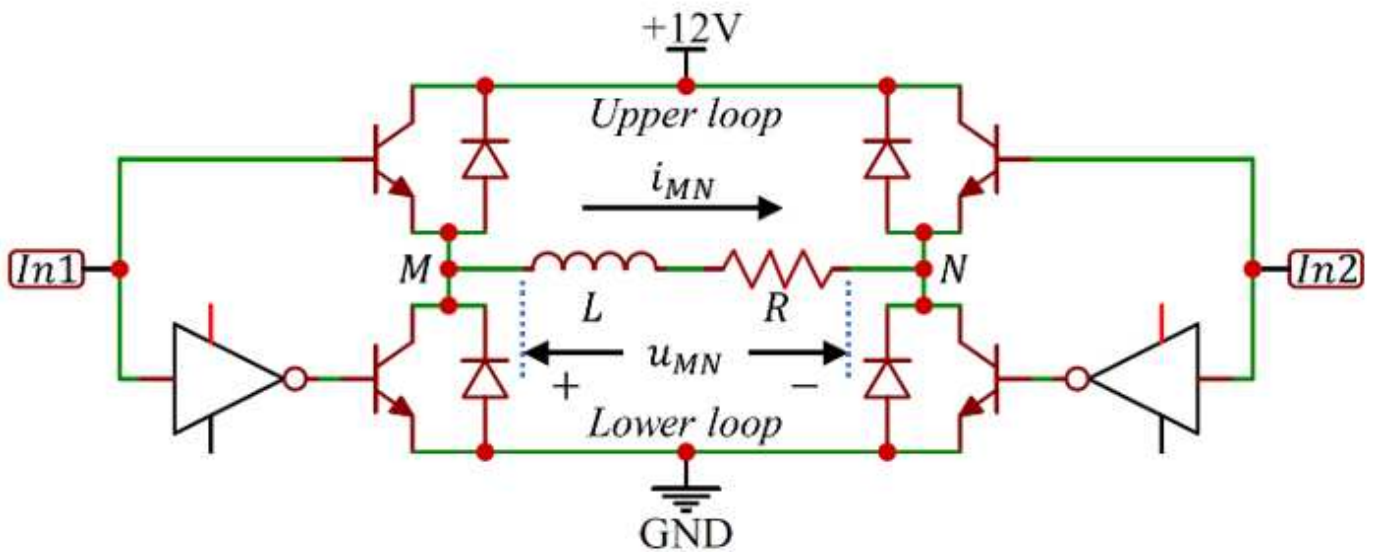


Figure 4

Electric circuit of L298N full-bridge PWM inverter.

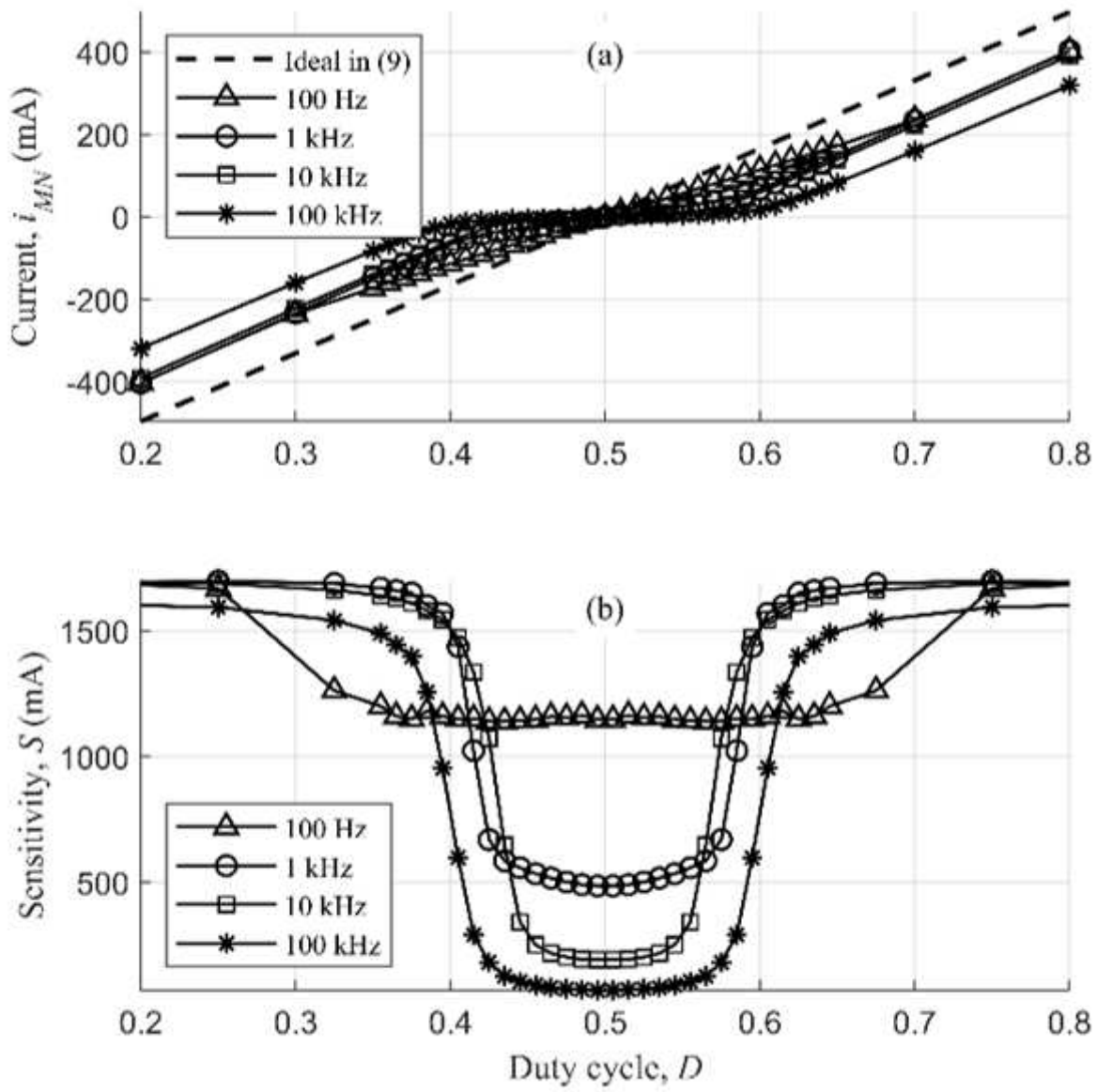


Figure 5

Variations of (a) i_{MN} and (b) S w.r.t. D for $f_{PWM}=0.1, 1, 10, 100$ "kHz".

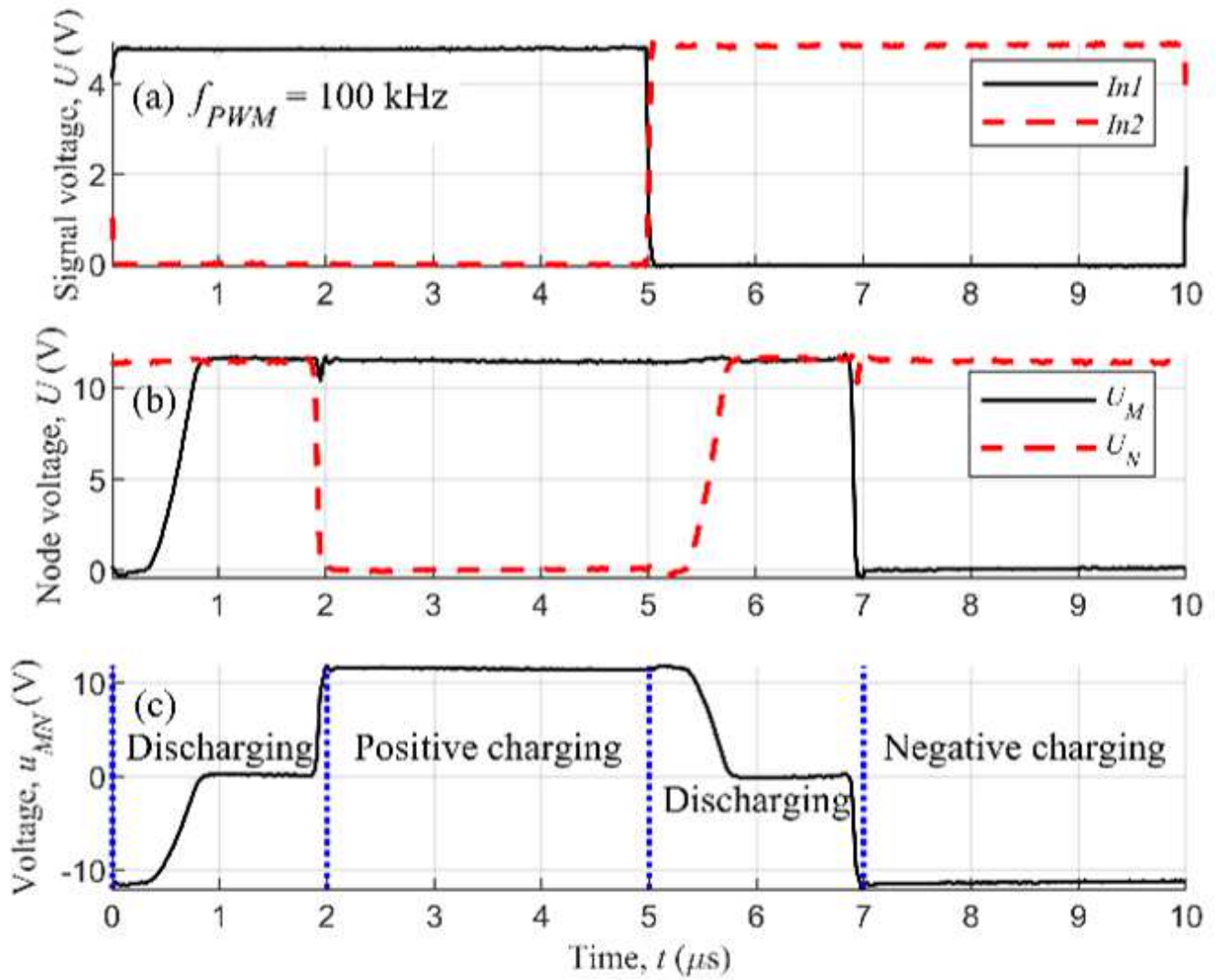


Figure 6

Whole-period variations of (a) $In1$ and $In2$, (b) U_M and U_N , and (c) u_{MN} for $f_{PWM}=100 \text{ kHz}$ and $D=0.5$ w.r.t. t . The $2 \mu\text{s}$ turn-off delay due to the IC L298N can be clearly observed for both U_M and U_N in (b). Three modes are highlighted in (c) according to u_{MN} .

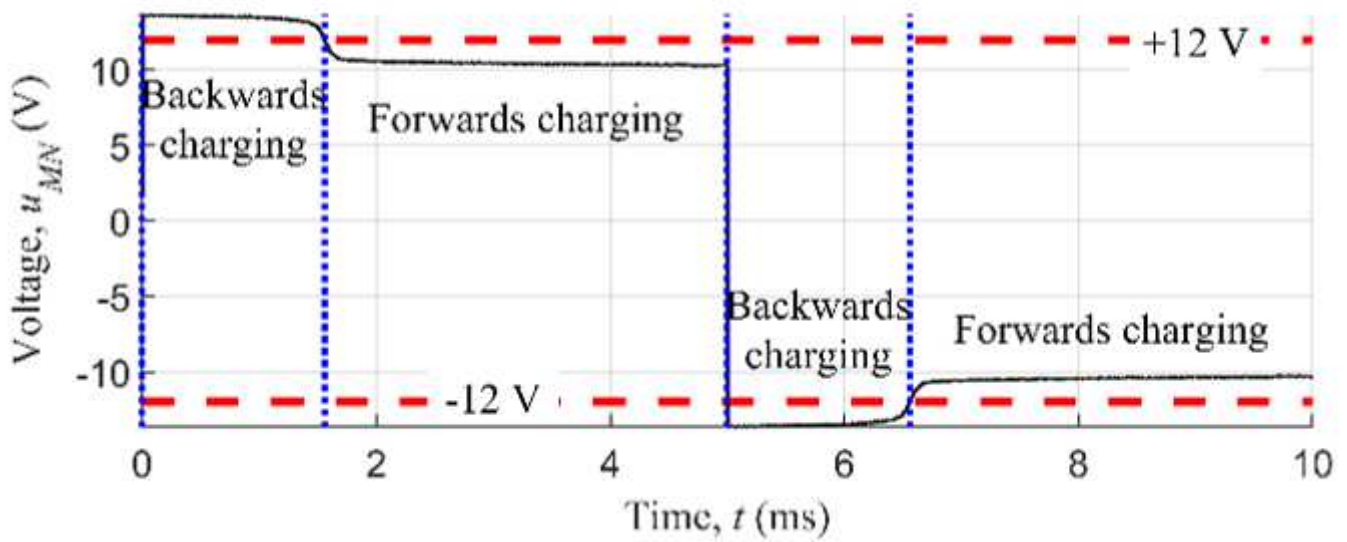


Figure 7

Whole-period variation of u_{MN} for $f_{PWM}=100$ "Hz" and $D=0.5$ w.r.t. t . The red dashed lines ($u_{MN}=\pm 12$ "V") indicate the boundaries between the FC and BC modes.

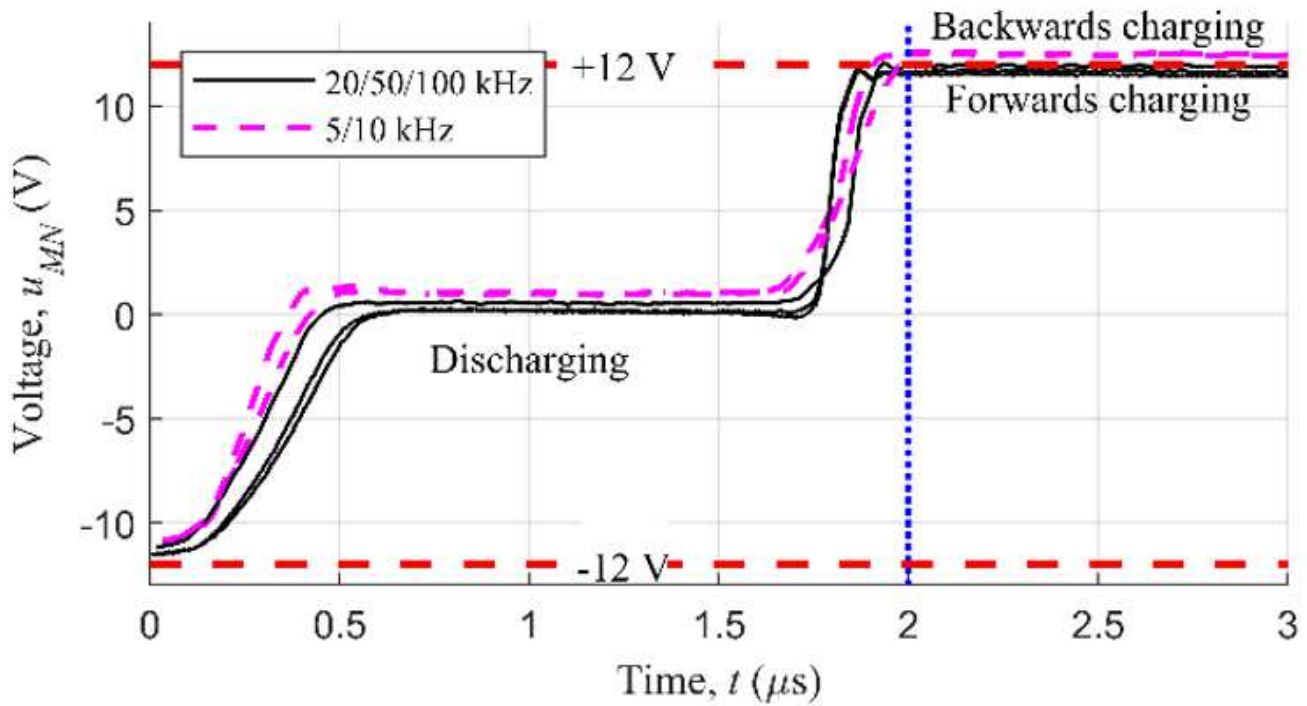


Figure 8

Initial-3- μ s variations of u_{MN} w.r.t. t for $f_{PWM}=5,10,20,50,$ and " 100 "kHz" and $D=0.5$.

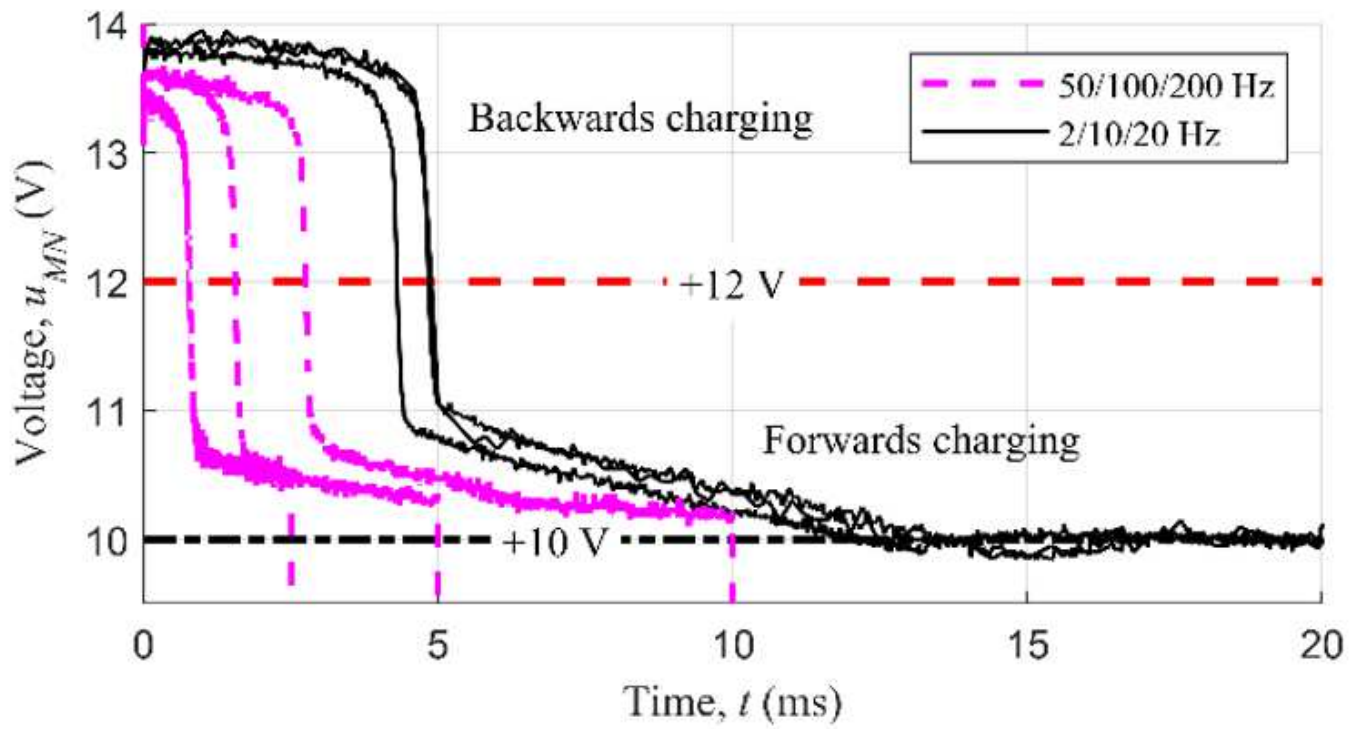


Figure 9

Initial-20-ms variations of u_{MN} w.r.t. t for $f_{PWM}=2,10,20,50,100,$ and " 200 "Hz" and $D=0.5$. Note that the 2 Hz and 10 Hz curves almost overlap with each other. The black dash-dot line ($u_{MN}=+10$ "V") indicates the saturation of the FC mode.

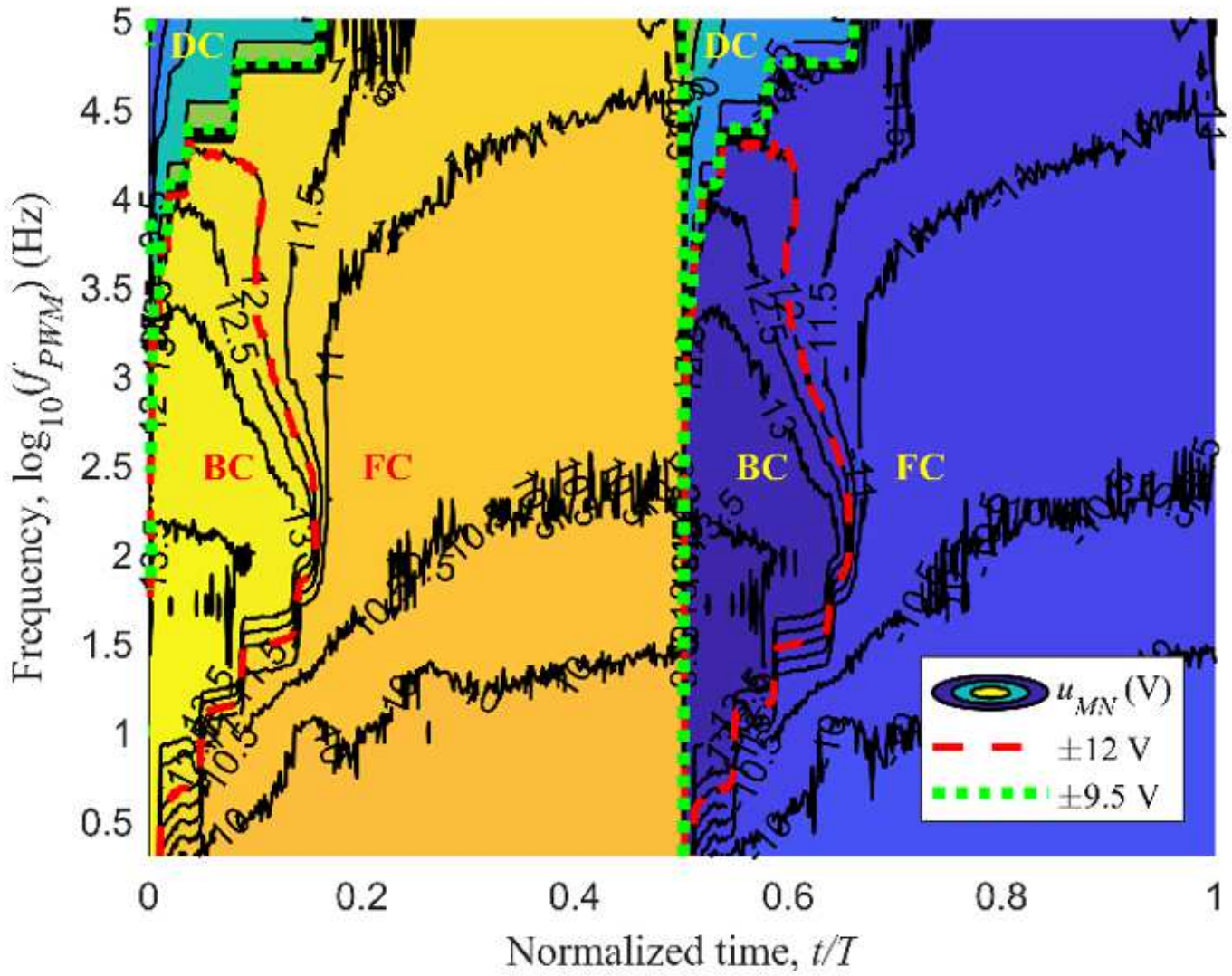


Figure 10

Contour of u_{MN} w.r.t. $\log_{10}(f_{PWM})$ and t/T for $D=0.5$. The green dotted curves ($u_{MN}=\pm 9.5$ "V") indicate the boundaries between the DC mode and the two charging modes.

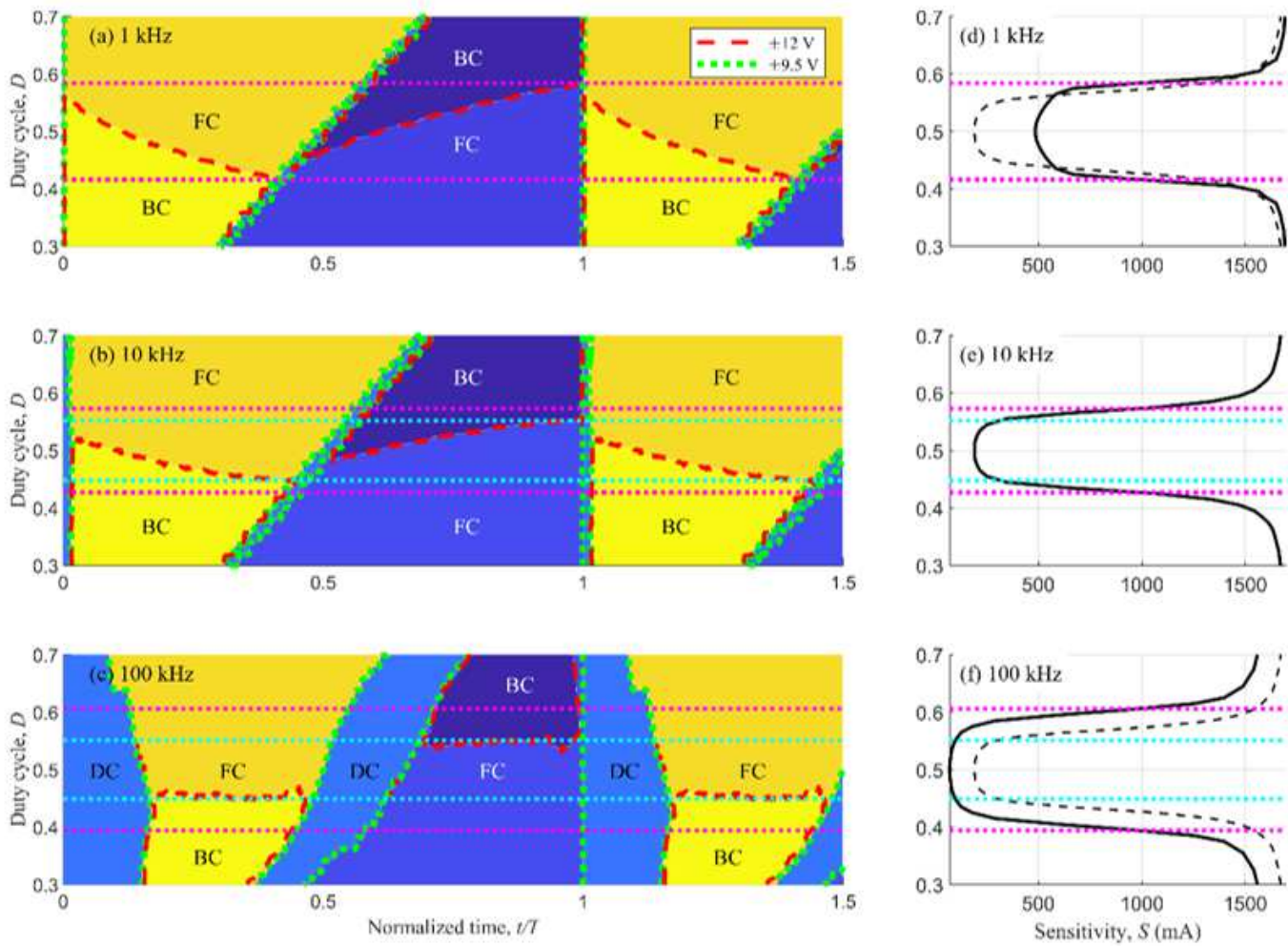


Figure 11

(a-c) Phase diagrams of u_{MN} w.r.t. D and t/T , and (d-f) variations of S w.r.t. D for $f_{PWM}=1, 10,$ and 100 "kHz". The cyan dotted lines indicate the termination points of the FC regimes, whereas the purple dotted lines indicate the transition points with $S=1000$ "mA". The dashed curve in (d&f) is the benchmark curve with $f_{PWM}=10$ "kHz".

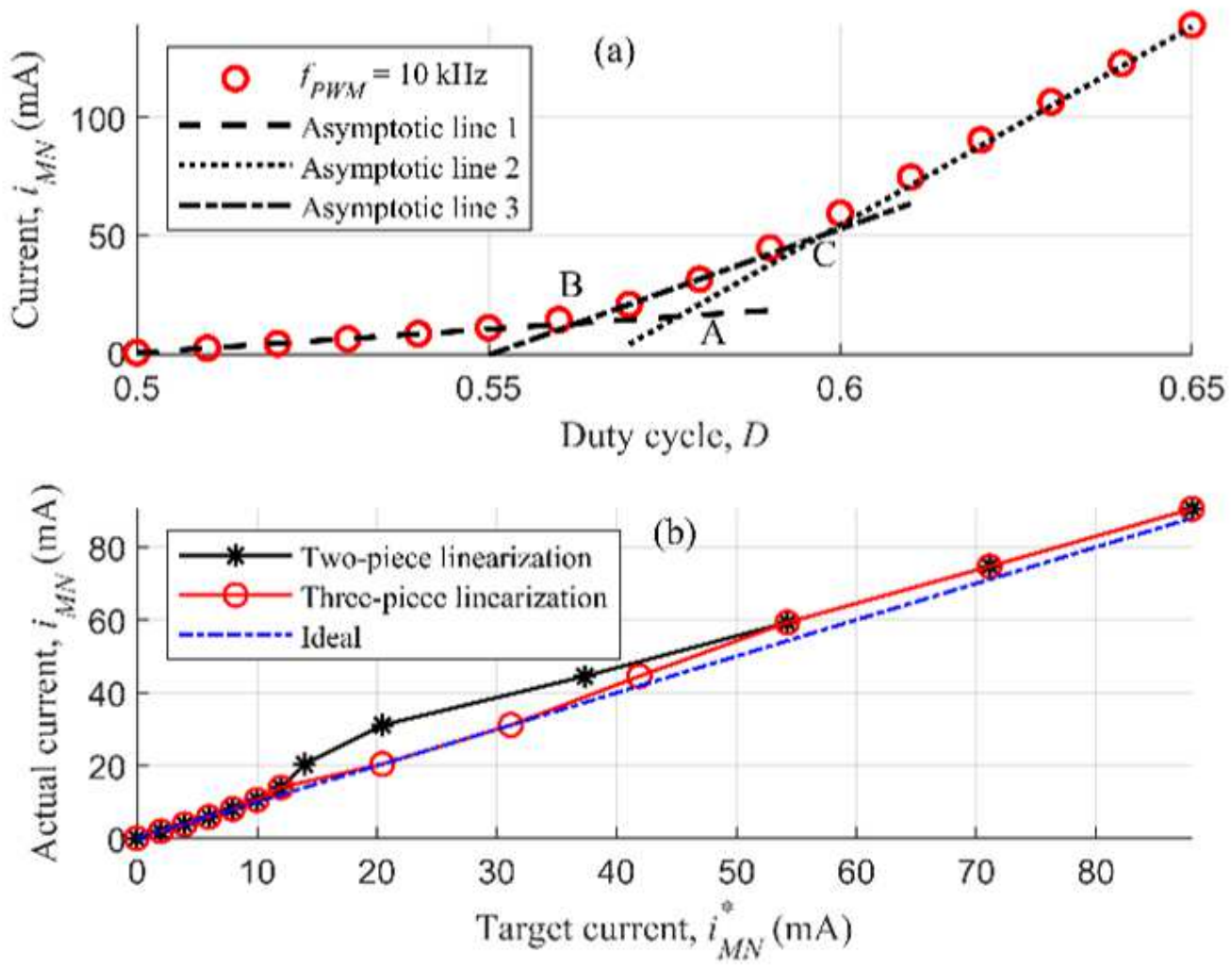


Figure 12

Variation of i_{MN} for $f_{PWM}=10$ "kHz" w.r.t. (a) D together with three asymptotic lines, and (b) i_{MN}^* for the two piecewise linearization approaches.

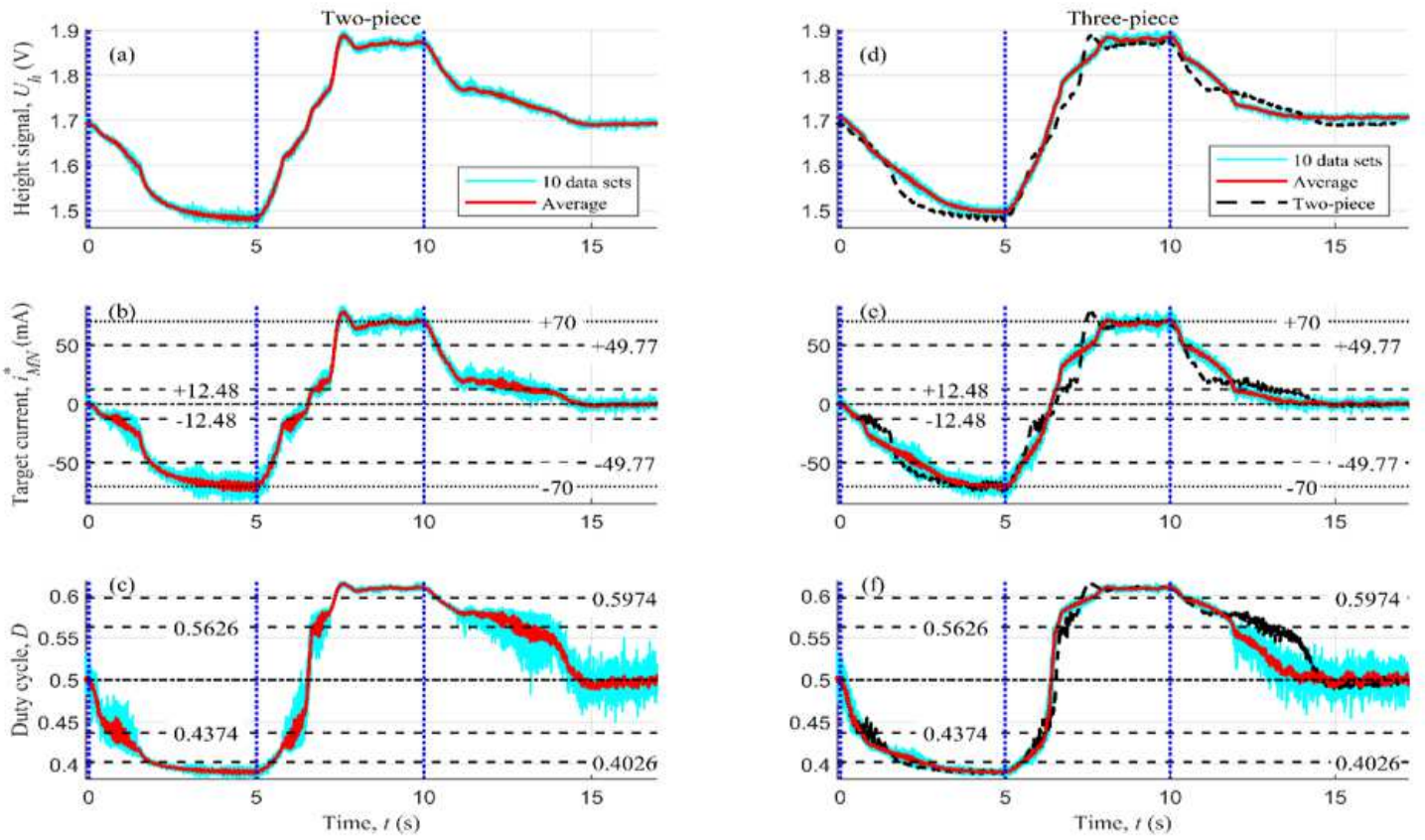


Figure 13

Experimental results of (a&d) U_h , (b&e) i_{MN}^* , and (c&f) D under the current-step-change test for $f_{PWM}=10$ "kHz" . The two columns correspond to the two-piece and three-piece linearization approaches, respectively. The cyan curves visualize ten repeats of the current-step-change test, whereas the red curves visualize the averaged value of the ten repeats. Intersection Points B and C, i.e., $(0.4374, -12.48 \text{ "mA" })$, $(0.5626, 12.48 \text{ "mA" })$, $(0.4026, -49.77 \text{ "mA" })$, and $(0.5974, 49.77 \text{ "mA" })$, are highlighted by horizontal black dashed lines.

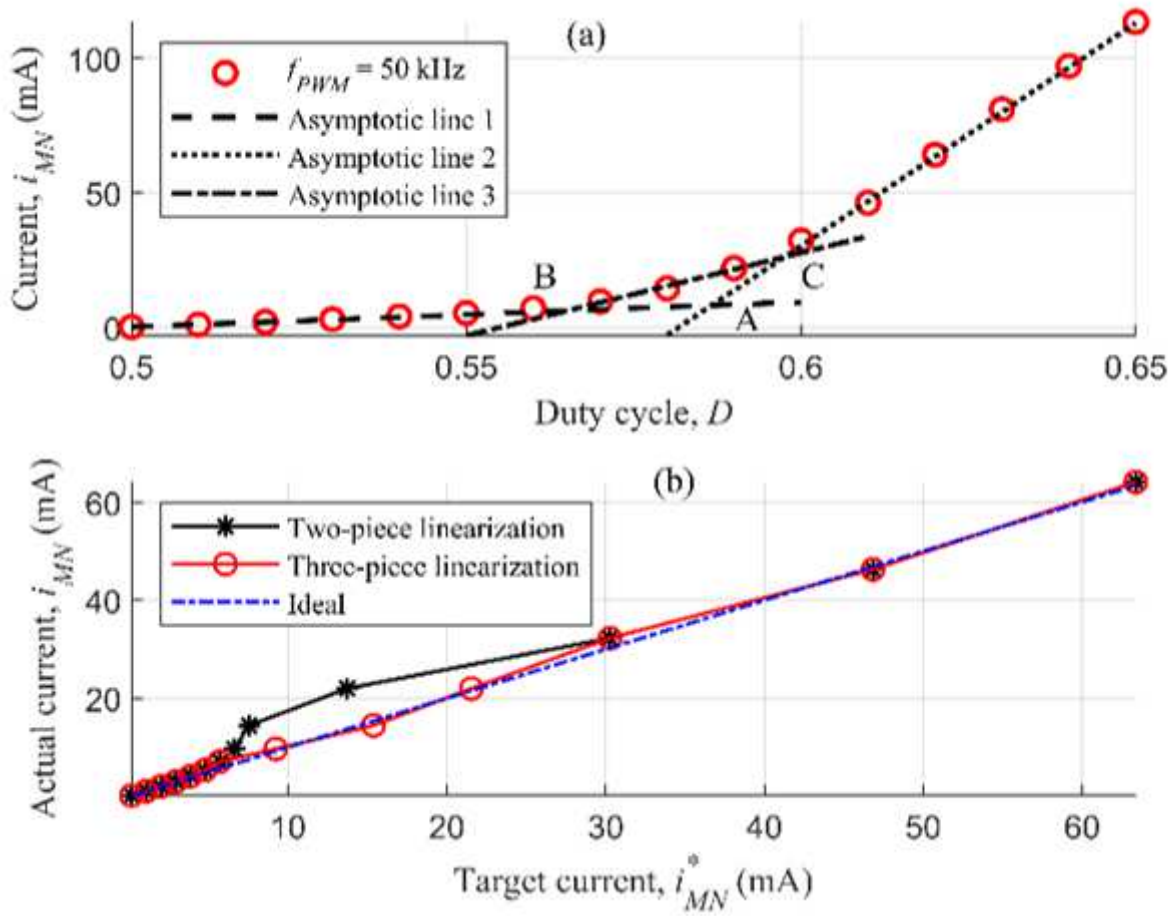


Figure 14

Variation of i_{MN} for $f_{PWM}=50$ "kHz" w.r.t. (a) D together with three asymptotic lines, and (b)

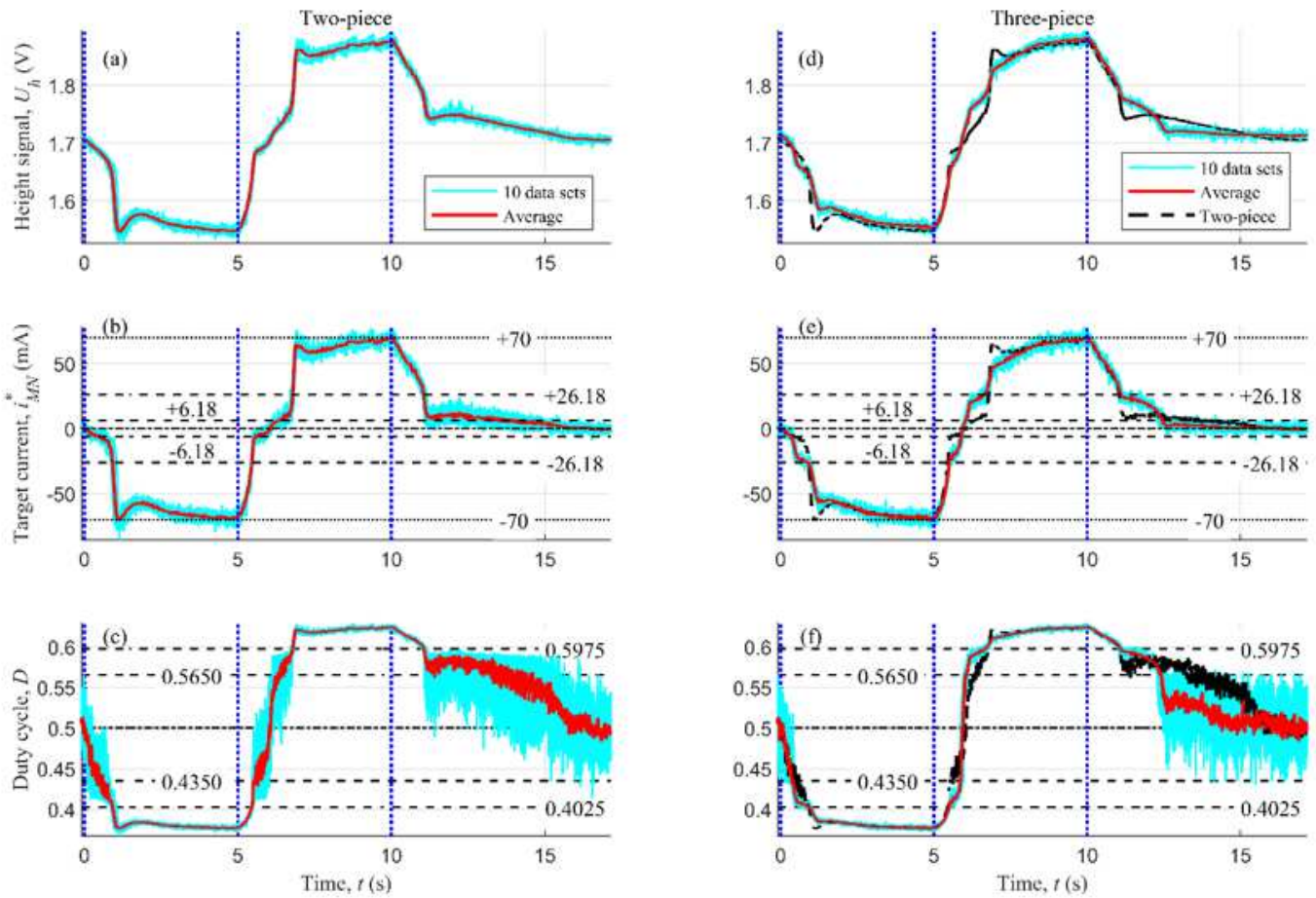


Figure 15

Experimental results of (a&d) U_h , (b&e) i_{MN}^* , and (c&f) D under the current-step-change test for $f_{PWM}=50$ "kHz". The two columns correspond to the two-piece and three-piece linearization approaches, respectively. The cyan curves visualize ten repeats of the current-step-change test, whereas the red curves visualize the averaged value of the ten repeats. Intersection Points B and C, i.e., $(0.4350, -6.18 \text{ "mA" })$, $(0.5650, 6.18 \text{ "mA" })$, $(0.4025, -26.18 \text{ "mA" })$, and $(0.5975, 26.18 \text{ "mA" })$, are highlighted by horizontal black dashed lines.

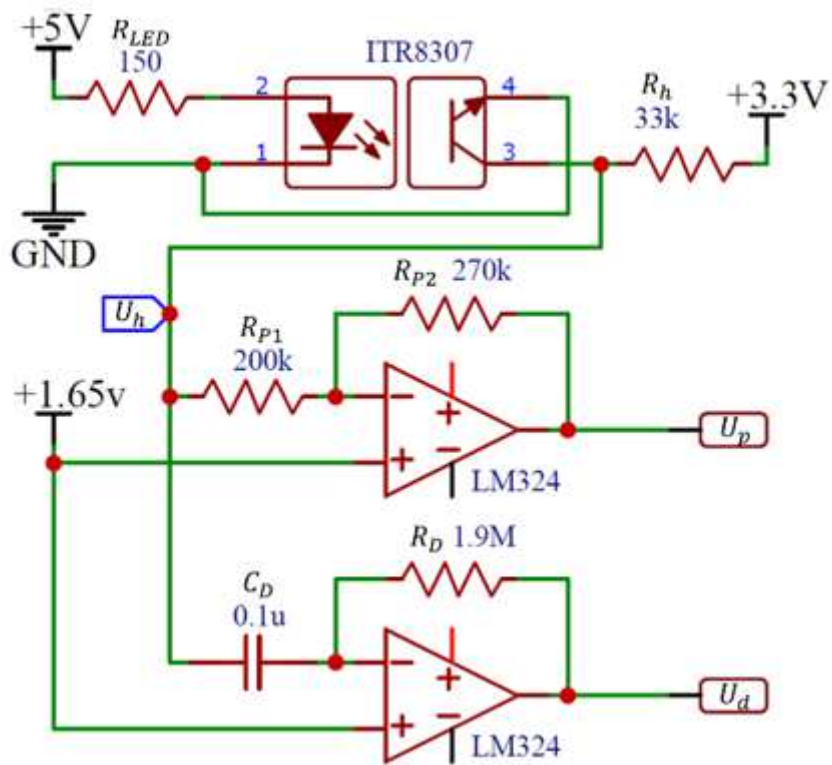


Figure 16

Electric circuit of the analog signal processor.

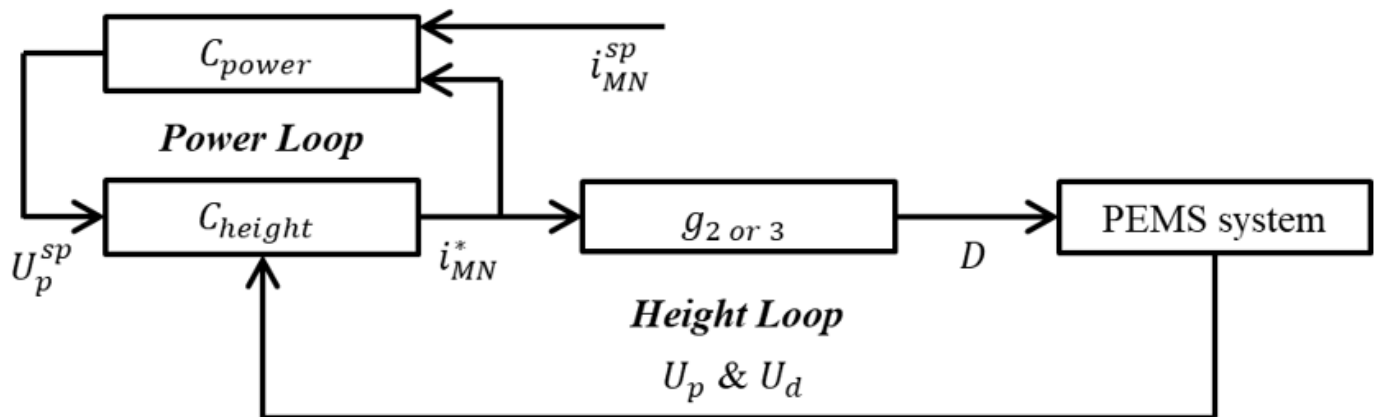


Figure 17

Double-loop block diagram for the STM32 controller.